FY22 STATUS REPORT: COLD SPRAY FOR CANISTER SCC MITIGATION AND REPAIR

Spent Fuel and Waste Disposition

Prepared for
US Department of Energy
Spent Fuel and Waste Science and Technology

Rebecca Schaller, Erin Karasz, Timothy Montoya, Jason Taylor
Sandia National Laboratories
Ken Ross
Pacific Northwest National Laboratories

September 1, 2022
M3SF-22SN010207055
SAND####

Sandia National Laboratories is a multimission laboratory managed and operated by National Technology & Engineering Solutions of Sandia, LLC, a wholly owned subsidiary of Honeywell International Inc., for the U.S. Department of Energy's National Nuclear Security Administration under contract DE-NA0003525.

DISCLAIMER

This information was prepared as an account of work sponsored by an agency of the U.S. Government. Neither the U.S. Government nor any agency thereof, nor any of their employees, makes any warranty, expressed or implied, or assumes any legal liability or responsibility for the accuracy, completeness, or usefulness, of any information, apparatus, product, or process disclosed, or represents that its use would not infringe privately owned rights. References herein to any specific commercial product, process, or service by trade name, trade mark, manufacturer, or otherwise, does not necessarily constitute or imply its endorsement, recommendation, or favoring by the U.S. Government or any agency thereof. The views and opinions of authors expressed herein do not necessarily state or reflect those of the U.S. Government or any agency thereof.

Prepared by
Sandia National Laboratories
Albuquerque, New Mexico 87185 and Livermore, California 94550

Sandia National Laboratories is a multimission laboratory managed and operated by National Technology and Engineering Solutions of Sandia, LLC, a wholly owned subsidiary of Honeywell International, Inc., for the U.S. Department of Energy's National Nuclear Security Administration under contract DE-NA0003525.

SUMMARY

This progress report describes work performed during FY22 at Sandia National Laboratories (SNL) to assess the corrosion performance of cold spray coatings to enable optimization of cold spray for the purposes of mitigation and/or repair of potentially susceptible regions, corrosion, or stress corrosion cracking (SCC) in austenitic stainless steel for spent nuclear fuel (SNF) storage. Of particular concern is SCC, by which a through-wall crack could potentially form in a canister outer wall over time intervals that may be shorter than possible dry storage times. In FY21, initial corrosion explorations of cold spray coating were evaluated and in FY22, an expanded set of cold spray coatings with in-depth analysis of post-exposure accelerated testing was explored. Additionally, relevant atmospheric exposure testing was carried out and initial results are presented herein. The corrosion attack from the accelerated testing and more realistic atmospheric exposures environments were compared to identify potentially deleterious factors for corrosion as well as help to understand the applicability of accelerated testing for cold spray optimization. This initial analysis will help to enable optimization of the corrosion resistance cold spray, one of the more promising coating and repair techniques, for potential application in an SNF environment. Learnings from both are summarized, and implications and future work are presented in this report.

ACKNOWLEDGEMENTS

The authors would like to acknowledge the following people for their contributions to the work documented in this report: Sandians Charles Bryan, Sara Dickens, Luis Jaregui, Jay Taylor, Makeila Maguire; Pacific Northwest National Laboratory contributors P. Mayur and B. Gwalani; and Ned Larson of the Department of Energy's Office of Nuclear Energy.

CONTENTS

This page is intentionally left blank.

LIST OF FIGURES

LIST OF TABLES

ACRONYMS

ASTM	American Society of Testing and Materials
BCC	Body centered cubic
BSE	Back scattered electron
CISCC	chloride-induced stress corrosion cracking
CrC	chrome carbide
CS	cold spray
DI	deionized [water]
DOE	US Department of Energy
EBSD	electron backscatter diffraction
EDS	energy-dispersive [X-ray] spectroscopy
FCC	Face centered cubic
FY	fiscal year
Inc	Inconel
ISFSI	independent spent fuel storage installation
NEUP	Nuclear Energy University Program
Ni	Commercially Pure Nickel
NRC	Nuclear Regulatory Commission
OCP	Open Circuit Potential
PNNL	Pacific Northwest National Laboratories
RH	relative humidity
SC	Super C
SCC	stress corrosion cracking
SEM	scanning electron microscope
SFWST	Spent Fuel and Waste Science and Technology
SNF	spent nuclear fuel
SNL	Sandia National Laboratory
SS	stainless steel

This page is intentionally left blank.

SPENT FUEL AND WASTE SCIENCE AND TECHNOLOGY

FY22 STATUS REPORT: COLD SPRAY FOR CANISTER SCC MITIGATION AND REPAIR

1. INTRODUCTION

In dry storage, spent nuclear fuel (SNF) is commonly stored in welded stainless steel (SS) canisters enclosed in passively ventilated overpacks. Over time, dust accumulates on the canister surfaces, and as the SNF cools, salts within that dust will deliquesce to form concentrated brines. If the salts contain aggressive species such as chloride, then the resulting brine can cause localized corrosion, and if sufficient tensile stresses are present in the metal, stress corrosion cracking (SCC) can occur. Over time, SCC cracks could penetrate the canister wall. Developing an improved understanding of the occurrence and risk of SNF storage canister SCC is considered to be significant to demonstrating the safety of long-term dry storage of SNF. For this reason, the Department of Energy (DOE) is funding a large effort to evaluate the occurrence and potential consequences of storage canister SCC as well as to develop prevention, mitigation, and repair technologies for this degradation mechanism, if it should occur.[1] This effort includes work at several different national laboratories and a large DOE-funded effort at universities, as part of the DOE Nuclear Energy University Program (NEUP) (Figure 1).

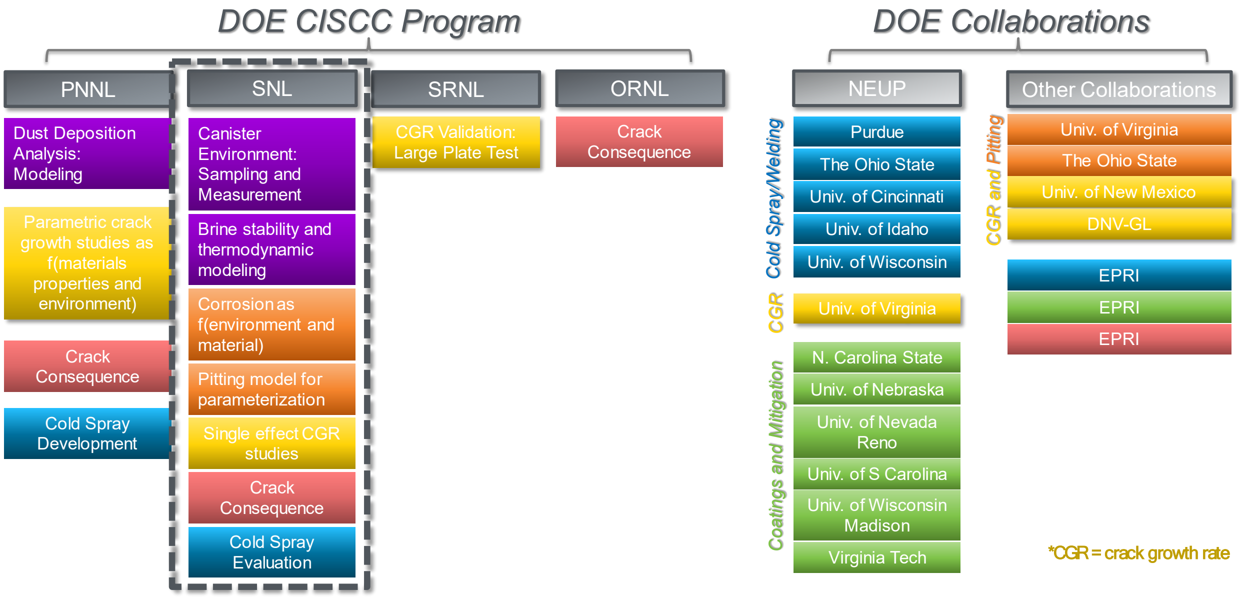

Figure 1. Experimental work on canister SCC currently being carried out by SNL, other national laboratories, and collaborators.

Sandia National Laboratory (SNL) plays a major role in this effort, leading many programs to develop an understanding of and evaluate the potential consequences of canister SCC. The chloride-induced (CISCC) SCC research at SNL involves many facets (as shown in Figure 2 and detailed in SNL's milestone reports -[2, 3]) but the focus of this milestone will be the work SNL is carrying out in collaboration with Pacific Northwest National Laboratories (PNNL) on the corrosion assessment of cold spray coatings for the prevention and mitigation of canister corrosion and SCC. It should be noted that the DOE has large NEUP efforts in corrosion coating development and an additional program at SNL in partnership with industry to develop other potential coatings solutions[1].

This report documents work done by SNL in collaboration with PNNL to begin to develop a scientific understanding of cold spray materials degradation behavior, specifically with respect to SNF relevant conditions. Both accelerated, American Society for Testing and Materials (ASTM) standardized testing, and relevant canister atmospheric exposure environments were explored to determine potentially deleterious factors and possible optimization pathways to enhance cold spray longevity.

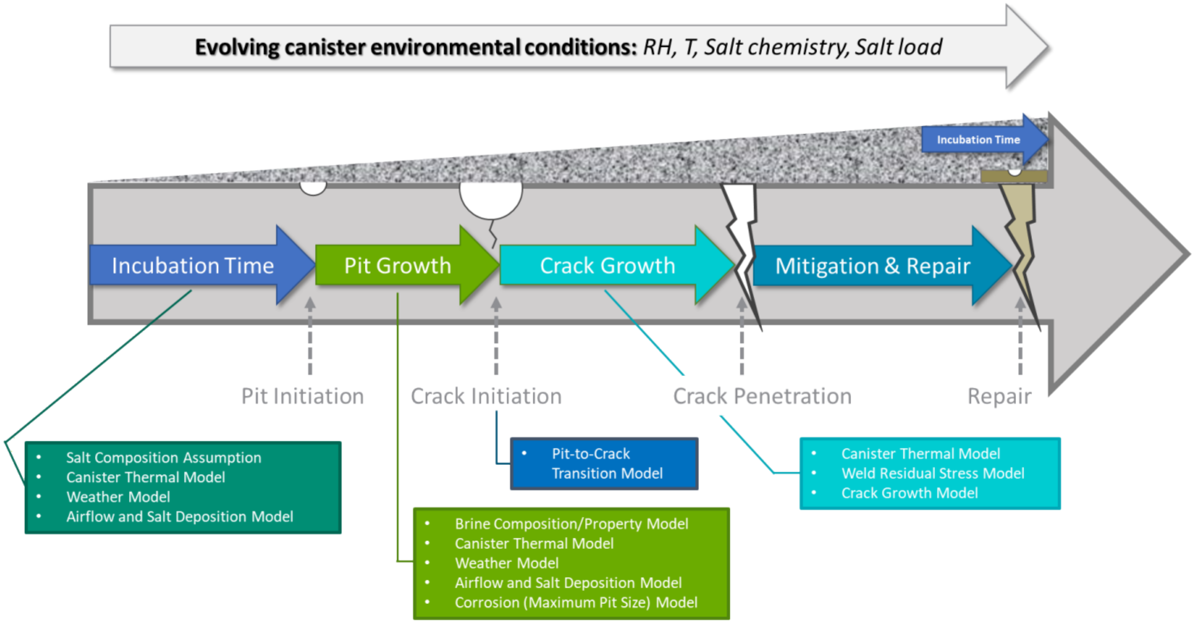

Figure 2. Program schematic detailing inputs for the probabilistic model for SNF dry storage canister SCC.

Cold spray is desirable as a coatings technique as it is a solid phase metal spray process during which no melting occurs. Metal particles are carried by a heated gas stream that softens the metal and propels particles at supersonic velocities towards a substrate. The impact energy is high enough to bond metal particles to the surfaces they impact. Because it is a solid phase process, cold spray avoids oxidation, tensile residual stresses, and other detrimental effects typical of the high heat input and melting associated with thermal spray. Cold spray can produce infinitely thick coatings with beneficial compressive residual stresses. Additional cold spray process details and best practices are more fully detailed in previous reports [4, 5].

1.1 Background

As discussed in the SNL FY22 report on corrosion resistant coatings[1], there are three main reasons why the application of a mitigation or repair strategy is unique for SNF canisters (as compared to other corrosion resistant coatings): 1) the dynamic and varied environment, 2) the space limitations/constraints for application, and 3) the necessity to comply with regulations and licenses set forth by the Nuclear Regulatory Commission (NRC). Additional challenges arise dependent on the intention or method of application of the cold spray. Three scenarios have been previously identified in the SNL FY 2020

Report on Corrosion-Resistant Coatings [3], and are discussed as ex-situ prevention, ex-situ repair, and in-situ repair, all of which have their own demands, some of which are detailed in Table 1.

Table 1. SNF canister SCC prevention and repair coating scenarios.

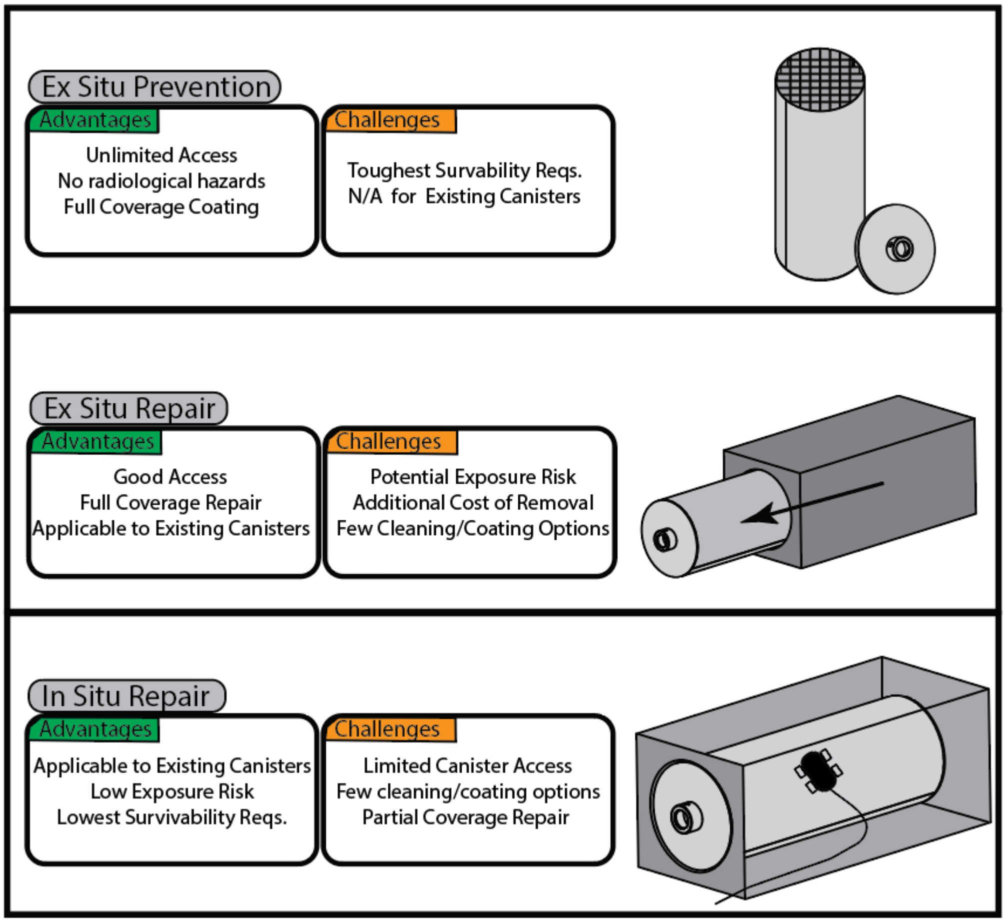

	Advantages	Challenges
Ex Situ Prevention	Unlimited Access No radiological hazards Full Coverage Coating	Toughest Survability Reqs. N/A for Existing Canisters
Ex Situ Repair	Good Access Full Coverage Repair Applicable to Existing Canisters	Potential Exposure Risk Additional Cost of Removal Few Cleaning/Coating Options
In Situ Repair	Applicable to Existing Canisters Low Exposure Risk Lowest Survivability Reqs.	Limited Canister Access Few cleaning/coating options Partial Coverage Repair

To date, acceptance criteria for any potential mitigation or repair strategy have yet to be defined. However, SNL seeks to better understand potential mitigation and repair strategies, the conditions and/or constraints that they will face during application, and their long-term materials degradation behavior. In selection of any potential strategy, these effects all must be considered, along with the notion that anything applied to the canister to protect from SCC, must first and foremost, “do no harm” to the integrity or materials lifetime of the canister itself. Cold spray, a low heat input, additive metals technology, has shown initial promise to both meet application needs for in-situ scenarios and have the initial desirable qualities to help prevent or repair canister SCC. SNL’s collaboration has focused on evaluating various cold spray coatings, using both accelerated ASTM standard tests for optimization and relevant atmospheric exposures for comparison. Additionally, as CS coatings may not be applied to the entire canister surface, either through a desire to protect only deleterious regions, such as welded regions and heat affected zones, or, due to physical constraints such as would be present in in-situ repair, edge effects may play a role in material lifetime performance. Therefore, a large part of SNL and PNNL’s work has focused on evaluating potential edge effects and understanding factors that may enhance optimization.

1.1.1 Cold spray

Since the 1980's, the additive manufacturing technique of cold spray has continued to be developed. In this technique, metal particles are accelerated by a stream of inert gas, such as nitrogen or helium, into a substrate material. The inert gas is heated, in order to achieve higher particle velocities, to temperatures below the melting temperature of the particles. These temperatures are usually under 1100 °C[6]. The metal particles adhere by a kinetic deformation process, distinguishing it from other thermal spray and additive manufacturing techniques that melt or sinter the particles.

The lower heat input can prevent temperature-dependent crystalline transformations,[7] and help prevent oxidation and vaporization[8]. The technique also creates coatings with other beneficial properties. Cold sprayed metals have high hardness values and generally good wear resistance[9, 10]. Cold spray induces compressive residual stresses which are often considered beneficial for preventing stress corrosion cracking[11, 12]. Cold spray has been applied to a variety of fields for an array of purposes: biocompatible medical implant coatings, military vehicle and aircraft repair, nuclear energy corrosion protection and wear resistance coating[13-15].

The use of cold spray as a corrosion mitigation and repair technique for SNF canisters is attractive as previous research has shown the capability for in-situ application[16]. Additionally, as it induces compressive stresses in the substrate, this is believed to be beneficial for reduction of susceptibility to corrosion and SCC. However, there are several known properties of cold spray that may need further consideration prior to implementation as a coating, particularly as a corrosion barrier such as in the case of SNF canisters. The potential for galvanic coupling effects between the selected cold spray material and the substrate cannot be ignored. Additionally, filler particles (such as hardening particles) and primary coating constituents may also introduce local or micro-galvanic couples. Porosity, a well-known corrosion initiator in AM materials [17-19], could also influence cold spray materials degradation. However, this has been shown fluctuate (with some controllability) with material selection and processing parameters[18-20]. The kinetic energy involved with the particle impact during cold spray deposition can create a nanocrystalline structure on the edges of the particles[21-23]. This impact also has the possibility to influence the underlying substrate microstructure, potentially leading to a martensitic shift, which could reduce the local corrosion resistance. Similar to other AM processes, residual stress is a concern[24, 25]. Even though cold spray induces compressive residual stress in the substrate directly beneath, it is unknown how compensation of this induced stress at coating edges may affect the distribution of residual stress and subsequent corrosion. While cold spray presents many beneficial properties that are desirable of a mitigation and repair strategy, it is important to evaluate known properties to ensure that any potential strategy applied to a canister "does no harm" with respect to corrosion and SCC resistance.

1.1.2 Summary of initial investigations from FY21

In FY21, cold spray samples were produced at PNNL with three spray material types, Inconel, Super C, and CP Nickel on SS304L and were sent to SNL for analysis. Nickel based alloys were selected as the first material system to explore for this study. All materials were deposited on SS304L base plates, as shown in Figure 3. As seen in Figure 3-b, the cold spray edge morphologies were tested in two configurations. Tapered edges refer to those that are untreated and allowed to build up a tapered edge between the cold spray and base material due to overspray with successive cold spray passes. Masked edges refer to cold spray edges that were masked during application, thus the edge exhibits a sharp, 90^o transition between the cold spray and base material. In addition to cold spray material differences and edge effects, samples provided by PNNL also employed two process gasses, He and N. A summary of the samples used in corrosion testing is provided in the following section with a full detailed report in the PNNL FY21 Year End Report [26]. Full immersion accelerated electrochemical testing and accelerated pitting evaluations were carried out on these samples. Additional subsets of the samples (in cases where a larger set was generated) were exposed under relevant atmospheric conditions as well as accelerated boiling $MgCl_2$ to evaluate susceptibility to SCC.

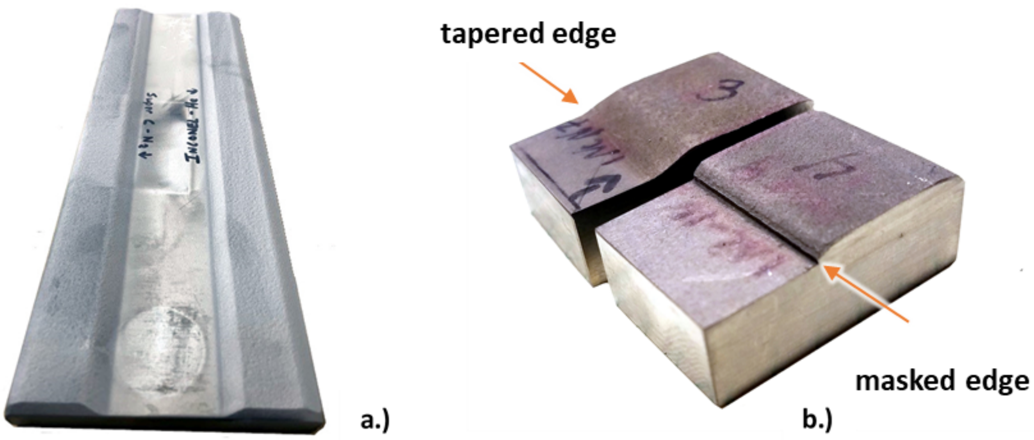

Figure 3. a) Cold spray plate and b) example edge geometries: tapered vs. masked.

1.1.3 FY22 developments and additional CS samples

In FY22, samples previously used for accelerated electrochemical testing in sodium chloride solution were polished and further examined in ferric chloride solutions for comparison to prior ferric chloride immersion pitting test results. Additionally, more in-depth analysis was performed on the samples that had been immersed in ferric chloride in FY21 to further understand the driving mechanisms for corrosion attack. Scanning electron microscopy (SEM) was performed on the top surfaces to interrogate the location of the attack in the interface region. Then the samples were cross-sectioned; optical imaging, SEM, and electron back-scatter diffraction (EBSD) were performed on the cross-sections. Particle size analysis was also conducted on the metal powders used to spray the samples tested previously in FY21. Nanoindentation for hardness measurements was also initiated to further expand the understanding of the relationship between material properties and corrosion susceptibility of the cold spray samples. Additional nanoindentation measurements are planned in FY23 to further explore this relationship.

The cold spray sample set tested originally in FY21 was also expanded in FY22 to include the samples listed in Table 2 below (these completed the initial matrix developed in FY21). Additionally, CS coatings developed with chrome carbide (CrC) hard particles were examined in FY22 (three variations of 316L + CrC as shown in Table 3). These samples were only examined in the accelerated pitting test (full immersion in $FeCl_3$) as only one sample of each spray condition/material type was received, and thus multiple tests were not possible. A full list of samples received from PNNL and characterized pre-exposure in FY22 are listed in **Error! Reference source not found.**. Continued testing of viable cold spray coatings will be carried out in FY23.

Table 2: Cold spray samples examined in accelerated corrosion testing in FY21 and FY22.

Cold Spray Material	Carrier Gas	Edge	Year
Inc	He	Tapered	FY21
Inc	N	Tapered	FY21
Inc	N	Masked	FY21
Ni	N	Tapered	FY21
Ni	N	Masked	FY21
Ni	He	Tapered	FY22
Ni	He	Masked	FY22
SC	N	Tapered	FY21
SC	He	Tapered	FY22
SC	He	Masked	FY22

Table 3. Cold spray coatings developed with hard particles and examined in $FeCl_3$ testing in FY22.

PNNL Sample No.	Powder	Carrier Gas Pressure (psi)	Carrier Gas Temp (C)	Carrier Gas	Carrier Gas Flow Rate (SLM)/feeder	Deposit thickness (mm)	Deposit thickness per pass (mm)
NE82-0018c	SS316 + 25% CrC 410	400	530	N	515	0.81	4.1
NE82-0020	SS316 + 25% CrC 410	600	650	N	714	1.02	4.8
NE82-0022	SS316 + 25% CrC 410	400	650	N	468	0.47	2.4

With expanded sample sets, additional exposures were introduced in FY22. An atmospheric exposure plan (based off of long-term corrosion exposure evaluations in the FY21 CISCC report) was developed and conducted on samples that had been received in FY21. Additionally, a subset of samples were exposed to ASTM G-36 (boiling $MgCl_2$ for SCC evaluation) in the as sprayed state. While samples were not stressed prior to ASTM G-36 exposure, the exposure allowed for examination of potential influences of residual stresses induced by the cold spray at the interface on the potential susceptibility to SCC.

2. Materials and methods

Wrought 304L, ½” thick plate, was used as the substrate material. The powders deposited were either Inconel 625-2 (Inc), Super C (SC), commercially pure nickel (Ni), or 316 stainless steel with CrC 410 hard particles. An example of a 304L plate after being cold sprayed is seen in Figure 3-a. The compositions are provided in Table 4. A sieving procedure was applied to reduce the variance of particle size and subsequent particle analysis was performed to evaluate the particle distribution (described in Section 2.1). Two edge types were employed: tapered and masked, seen in Figure 3-b. In tapered edge samples, the cold spray tapers down from the full height of the coating to the substrate (due to overspray during the process) while in the masked edge, the cold spray drops off sharply. Samples of both edge types were tested for all material and gas combinations except Inconel-helium, Super C- nitrogen, and those with the CrC hard particles, for which only tapered interface samples were available.

Table 4: Compositions in weight percent for cold spray powders compared to the 304L base material used in this study.

	Inconel 625-2	**Super C**	**Ni**	**316L**	**CrC 410**	**304L Base Material**
C	0.02%	0.02%	≤0.01%	≤ 0.03%	4%	0.025%
Co	0.09%	0.2%	-	-	-	-
Cr	21.47%	23.2%	-	16-18%	Balance	18.19%
Ni	Balance	Balance	>99.9%	10-14%	8%	8.05%
Mo	9.06%	17.7%	-	2-3%	-	0.27%
Mn	0.04%	0.7%	-	≤ 2%	-	1.30%
P	0.0%	0.002%	-	≤ 0.045%	-	0.028%
S	0.0%	0.004%	≤0.001	≤ 0.03%	-	0.001%
Si	0.07%	0.5%	-	≤ 1%	-	0.34%
Fe	4.62%	0.6%	≤0.14%	Balance	-	-
Al	0.04%	-	-	-	-	-
B	0.001%	0.003%	-	-	-	-
Nb	3.65%	-	-	-	-	-
O	0.024%	-	≤0.4%	≤ 0.1%	-	-
V	-	0.30%	-	-	-	-
W	-	0.26%	-	-	-	-
N	-	-	-	≤ 0.1%	-	0.070%
Cu	-	-	-	-	-	0.36%

2.1 Cold spray materials characterization

Prior to the deposition process, cold spray powders are routinely dried and sieved to provide the highest fidelity coatings. Powder used for the Inconel and Super C samples was obtained after the sieving process and analyzed using a Microtrac-Retsch Camsizer M1 to ascertain the particle size and distribution. In this technique powder is dispersed onto a glass slide using the M-Jet dispersion unit. An automated light microscopy analysis is applied to backlight the particles and create shadows for size analysis. Approximately 14,000 and 18,000 particles were analyzed respectively. Particle sizes are reported as particle area (which can be used to calculate a circle-equivalent diameter). For reporting and comparison, d10 refers to the diameter of a particle in the 10th percentile, d50 refers to a particle in the 50th percentile (or median), and d90 refers to a particle in the 90th percentile.

The coatings were analyzed for porosity and surface roughness. Surface roughness measurements were taken with a Keyence VR-5200. The porosity was evaluated following ASTM-E2109-01[27]. A minimum of three optical micrographs were collected for each sample type following cross-section and polishing. The micrographs were collected at similar magnifications and analyzed using the Image J software[28].

2.2 Corrosion evaluation

Much of the corrosion testing conducted In FY22 utilized the same techniques as outlined in [2]. Two accelerated ASTM standard tests were applied for evaluation of the cold spray material, except in the case of the CrC samples, which were only exposed in ASTM G-36, as only one sample of each condition was supplied by PNNL. Electrochemical testing was conducted in 0.6 M NaCl and in FY22 additional testing in ferric chloride were added. Ferric chloride pitting corrosion tests followed ASTM G48 method A[29]. In FY22 atmospheric exposures and boiling magnesium chloride exposures, ASTM G36-94[30], were explored to evaluate the cold spray corrosion response and SCC susceptibility. Sample exposure sets for these additional tests were built off of the remaining cold spray samples delivered in FY21 as multiple duplicate samples were provided for these. Samples supplied in FY22 did not have sufficient duplicates to expand exposure methods to these additional tests.

2.2.1 Accelerated testing - electrochemical methods

Samples were tested in the as-sprayed and ground conditions. The substrate material was also tested for comparison purposes. Ground samples were ground with silicon carbide paper to 600 or 1200 grit finish, rinsed with DI water, and dried with nitrogen. An o-ring with an area ranging from 0.1 to 0.3 cm^2 was fixed to the sample surface using DevCon 5-minute epoxy. Each surface condition was examined a minimum of three times per sample. The approximate locations of each polarization scan on the cold spray are shown in Figure 4. The opposite side of the o-ring was then epoxied onto a flat cell and the sample, o-ring, and flat cell endcap were secured with a clamp. The flat cell was filled with aqueous 0.6 M NaCl or 6% by mass ferric chloride solution (noted later when scans are presented). A counter electrode of platinum-niobium mesh and an Ag/AgCl reference electrode were used. Potentiodynamic scans were run on a Biologic SP-300 potentiostat. The cold spray or base material samples were first allowed to equilibrate at the open circuit potential (OCP) for one hour, followed by an anodic scan starting from -0.2 V vs OCP to 0.8 V vs Ag/AgCl at a scan rate of 0.167 mV/s. A cut-off current of 100 μA was employed during the potentiodynamic scan. Post potentiodynamic-testing, the exposed surface area was measured optically on a Keyence VHX-7000 Digital Microscope and the reported current density was normalized by this area. For the additional open circuit potential holds conducted on the FY21 samples, samples were polished to 1200 grit, and exposed in 6% by mass ferric chloride solution following the same procedure as the scans in 0.6 M NaCl.

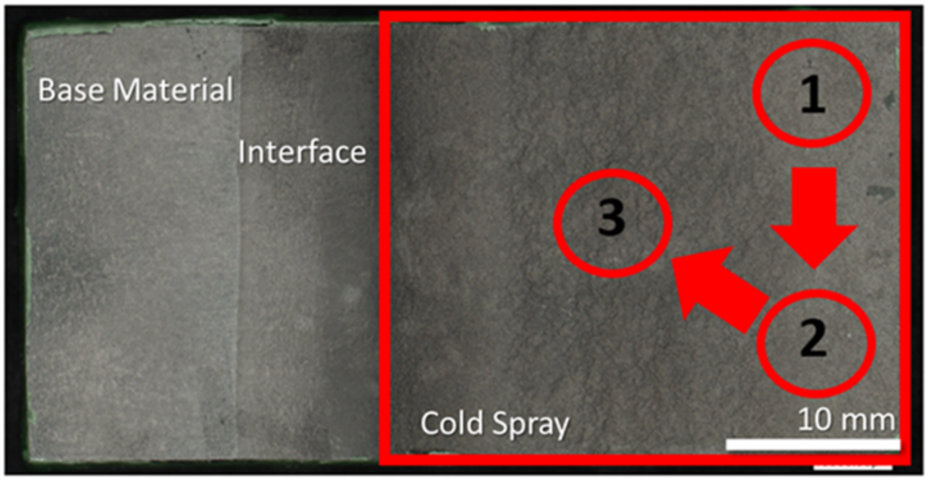

Figure 4: Cold spray sample with the cold spray region outlined in red (to the right). The circles within the cold spray region indicate the approximate locations of electrochemical testing.

2.2.2 Accelerated testing – full immersion pitting examination

Accelerated full immersion pitting tests were performed in accordance with the ASTM G48 method A[29]. The sides and bottom of the cold spray samples were coated in epoxy, seen in Figure 5. All samples were optically imaged pre-exposure on a Keyence VHX-7000. Samples were submerged in 6% by mass ferric chloride solution at 22 °C for 72 hours. At the conclusion of the test, samples were rinsed with DI water and dried with nitrogen gas. Samples were again optically imaged on a Keyence VHX-7000. Higher resolution images of the exposed surface were acquired with a Zeiss Gemini 500 Field Emission Scanning Electron Microscope. The samples were then cross-sectioned and the cut surface (perpendicular to the exposed cold spray) was polished to a mirror finish and imaged with a Keyence VHX-7000. Additionally, electron backscatter diffraction (EBSD) was performed on the cross-sections. At the resolution examined, diffraction patterns in the cold spray were unobtainable due to the substantial deformation of the cold spray particles. As a result, EBSD focused on two primary areas, first on the substrate immediately beneath the patch edge and second, on a region under the full coating thickness, far from the edge and therefore far from any potential corrosion damage. An additional set of samples developed with CrC hard particles (as shown in Table 3) were also exposed in the $FeCl_3$ solutions.

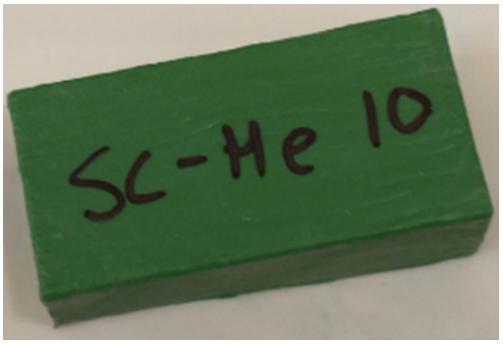

Figure 5: Bottom view of a sample coated in epoxy prepared for exposure in $FeCl_3$ solution.

Note: The ASTM G48 method A standard is applied for pitting analysis. These tests were undertaken to develop an understanding of pitting resistance across the interface of both the cold spray and base material. Observations of crevices are noted in the results of this pitting test (seen in sections 3.2.2 and

3.2.3). However, further examination in relevant atmospheric exposures (as described in the subsequent section and initiated in FY22) is needed to determine if this attack morphology is also observed under atmospheric conditions.

2.2.3 Relevant atmospheric exposure corrosion evaluation

Atmospheric exposures were conducted under both static and cyclic conditions on the samples listed in Table 5. These samples were selected for exposure as they were the only samples received with multiple samples for the same spray conditions and materials, of which only the Ni N masked samples had a sufficient set to expose under all desired exposure conditions. The cyclic conditions were based on ambient RH and temperature measurements taken near the Arkansas Nuclear 1 nuclear power station, and then modified to mimic the conditions on the surface of a heated SNF dry storage canister [2]. Both RH and temperature fluctuate, passing through the deliquescence point for $MgCl_2$ salt. Low and high humidity static exposures, one below the deliquescence point of NaCl and one above, were selected for comparison[31]. Prior to exposure, 300 $\mu g/cm^2$ of artificial sea water was printed on the samples (across the base material, interface, and cold spray surface) for atmospheric testing. Samples were periodically pulled throughout the duration of the exposure (4, 8, and 10 weeks) and imaged using the Keyence VHX-7000 optical microscope. At the end of exposure, samples were removed and are currently being processed for further corrosion characterization (SEM and cross-sectioning). Initial SEM top-down images are presented herein.

Table 5. Exposure list for atmospheric exposure testing and boiling $MgCl_2$.

Cold Spray Sample	Atmospheric Exposure			Boiling $MgCl_2$ Exposure
	40 % RH, 35 °C	75 % RH, 35 °C	Cyclic	
Inc He Tapered	1	-	1	1
Inc N Tapered	-	-	1	1
Inc N Masked	1	1	1	1
Ni N Tapered	1	-	1	1
Ni N Masked	1	1	2	1
SC N Tapered	1	1	1	-

2.2.4 Accelerated testing – boiling $MgCl_2$ for SCC evaluation

A subset of available samples, as noted in Table 5 were exposed according to the ASTM G-36 procedure for evaluation of susceptibility to SCC. While the samples were not exposed with an externally applied stress, the cold spray process itself, due to the high velocity particle impact, induces residual stress in the substrate. While these stresses are expected to be compressive underneath the cold spray, it is unknown how compensation for these stresses at the edge of a patch (colds spray and base material interface) may act, and in turn, may affect the resistance of the edge to SCC. Cold spray samples were coated on the sides and bottom with epoxy, in the same manner as samples prepared for the ferric chloride testing, thus leaving the interface exposed. Samples were then imaged pre-exposure using the Keyence VHX-7000 optical microscope. Samples shown in Table 5 were then immersed in saturated boiling $MgCl_2$ at 155 °C, following ASTM G36-94[30]. Samples were optically examined every 24 hours for evidence of SCC. In the absence of any readily apparent damage, samples were exposed for a total of a week. Samples are currently under preparation for further examination of corrosion damage. Initial post-exposure optical images are presented herein.

2.3 Metallurgical evaluation

Pre and post-exposure, the surfaces of the cold spray samples, from the base material to the cold spray, were optically imaged. Top-down optical microscopy was carried out using a Keyence VHX-7000, both pre- and post-exposure. Scanning electron microscopy of the post-exposure samples was conducted, as detailed in [2]. Samples were then cross-sectioned and the face perpendicular to the cold spray surface was polished with silicon carbide paper. Optical images of the cross-sections (perpendicular to the cold-sprayed surface) were taken using the Keyence. The set of samples tested in FY21 were polished further to an EBSD-quality finish. SEM and EBSD were conducted at the corroded patch edge, as well as a region further under the patch, far from the corrosion damage.

Nanoindentation was also conducted on the cross-sections from the FY21 sample set. Nanoindentation was conducted using a Bruker Hysitron TI 980 with a diamond Berkovich tip with a ½ angle of 65.25 ° at a force of 10,000 µN. Initial results are presented herein, with further analysis to be carried out in FY23.

3. Results and discussion

3.1 Materials characterization

The powder analysis revealed that post-sieving, there was a Gaussian distribution of particle size for both the Super C and Inconel powders. The Super C powder was slightly larger than the Inconel powder. Both powder samples were spherical in nature. The associated measurements are provided in Table 6.

Table 6. Measured particle size and sphericity measurements for the Inconel and Super C powders post-sieving procedure.

	Inconel	**Super C**
D_{10}	20.6 µm	24.5 µm
D_{50}	31.8 µm	37.1 µm
D_{90}	44.8 µm	50.9 µm
Sphericity	0.88	0.87

For the Inconel and nickel cold spray coatings, the processing gas produced noticeably different levels of porosity with the helium producing much lower porosity (Table 7). In the case of the Super C, the porosity is not substantially different between processing gases. Use of helium led to slightly smoother surfaces for the Super C and Inconel samples, but a drastic decrease in surface roughness was observed for the nickel coating.

Table 7: Porosity and surface roughness measurements for samples exposed in FY21 & FY22.

Sample	**Porosity (%)**	**S_a (µm)**
SC-He	5.26 ± 0.11	12.6 ± 1.5
SC-N	5.51 ± 0.44	16.7 ± 0.5
Inc-He	1.21 ± 0.20	15.7 ± 0.5
Inc-N	5.79 ± 0.18	17.2 ± 0.6
Ni-He	0.89 ± 0.38	3.5 ± 0.8
Ni-N	3.78 ± 0.59	18.5 ± 0.6

3.2 Accelerated corrosion examination results

3.2.1 Accelerated testing - electrochemical methods

Potentiodynamic scans were conducted in 0.6 M NaCl solutions on the samples listed in Table 2 and plotted along with the data obtained previously in FY21. Figure 6-a shows the open circuit potential hold on the as-sprayed surface. All samples had higher open circuit potential values compared to the 304 substrate material. Figure 6-b and c show the potentiodynamic scans for the as-sprayed and polished conditions. In all cases, polishing reduced the instances of metastable pitting (seen as sharp increases in current on the polarization curves in b, but are absent in c). The breakdown potential of the nickel sample remains low in both as-sprayed and polished conditions for the helium processed condition (roughly between 200 and 400 $mV_{Ag/AgCl}$ whereas the other samples did not display a breakdown over the potentials examined). The samples processed with helium, which have lower porosities, exhibit in general lower passive current densities for the polished surfaces.

Additionally, open circuit potentials and potentiodynamic polarizations were collected for the cold spray coating material in 6% by mass ferric chloride solution. Potentiodynamic polarizations in the solution were attempted but displayed active behavior and readily corroded through the cold spray material, thus are not reported herein. However, OCPs were collected, and in all cases, the coatings displayed a significantly higher OCP than the base material (Figure 7). This indicates, that even in the aggressive $FeCl_3$ solution, the role of the galvanic couple between the base materials and the cold spray coating could influence the corrosion behavior.

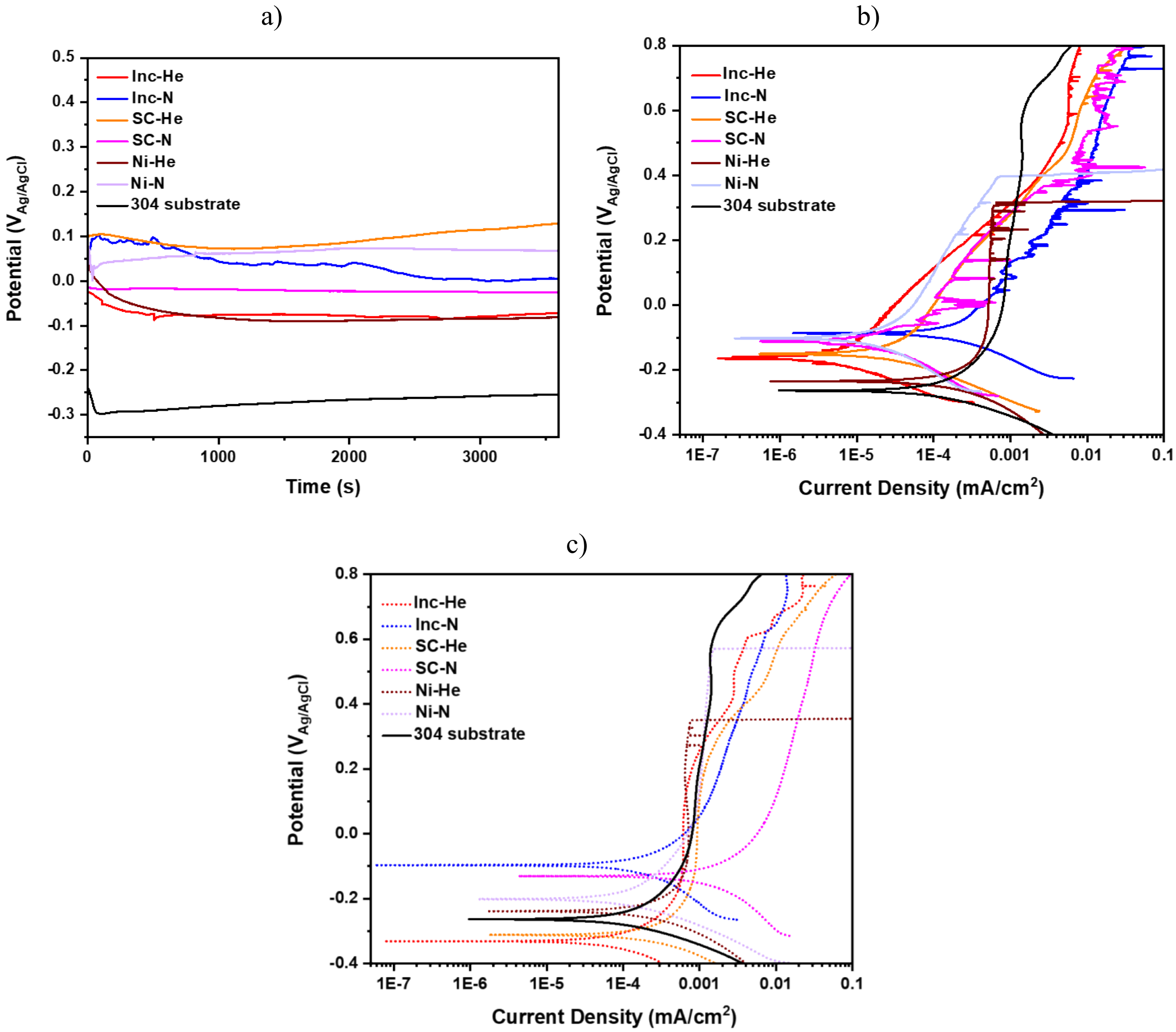

Figure 6: (a) Open circuit potential hold and (b) potentiodynamic scan for as-sprayed condition cold spray samples and (c) potentiodynamic scans for samples polished to 1200 grit. All scans were conducted in 0.6 M NaCl solution and are compared to the base material (black).

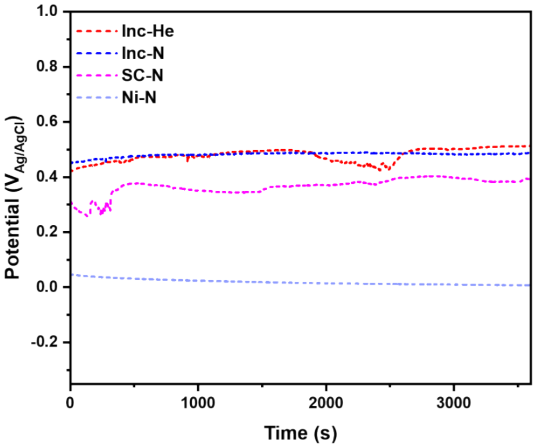

Figure 7: Open circuit potential hold in 6% by mass ferric chloride solution for polished cold spray samples.

3.2.2 Accelerated testing – full immersion pitting examination

Examples of optical top-down optical images before and after accelerated pitting tests of ferric chloride exposure are shown in Figure 8. While it is difficult to observe the corrosion damage optically, it is apparent that enhanced attack occurs at the interface. Additionally, in the case of the Ni N masked cold spray, attack of the coating can also be observed. Figure 9 contains post exposure optical images for all samples. Optical observations of the Ni-N samples display that they sustained quite a bit of damage in the cold spray region, while other cold spray materials were not visibly damaged. Specifically, it is difficult to determine through optical evaluation if any corrosion damage occurred on the Inc-N tapered, Inc-He tapered, and SC-N tapered (Figure 9-a-d). Heavy pitting sustained right at the interface appears for both nickel tapered samples appears in these images as a light line at the junction between cold spray and substrate (Figure 9-g&i). Some dark spots, indicative of corrosion attack at the interface are visible for the masked samples, and appear at the patch edge for the masked samples (Figure 9-f,h,&j).

A Note on the $FeCl_3$ accelerated tests: Direct comparisons are difficult to make between the samples exposed in FY21 (all nitrogen processed samples and the Inc-He sample) and the remaining He processed samples. As these samples were exposed at two different time periods, the chemicals used to make the ferric chloride solution were from two different containers. The first set was prepared with a previously purchased $FeCl_3$, which over its lifetime, as it is a hydrophilic chemical, likely absorbed some water, hence, when mixed by weight, could have been slightly more dilute than the target concentration of 6%. The second batch, while still prepared to the ASTM standard, was exposed to solution made from a freshly opened $FeCl_3$ chemical, thus the concentration of the second exposure may be slightly more aggressive in comparison as less water had been absorbed. Similar trends can be observed in both exposures, and inferences can be made, however care has to be taken for direct comparison.

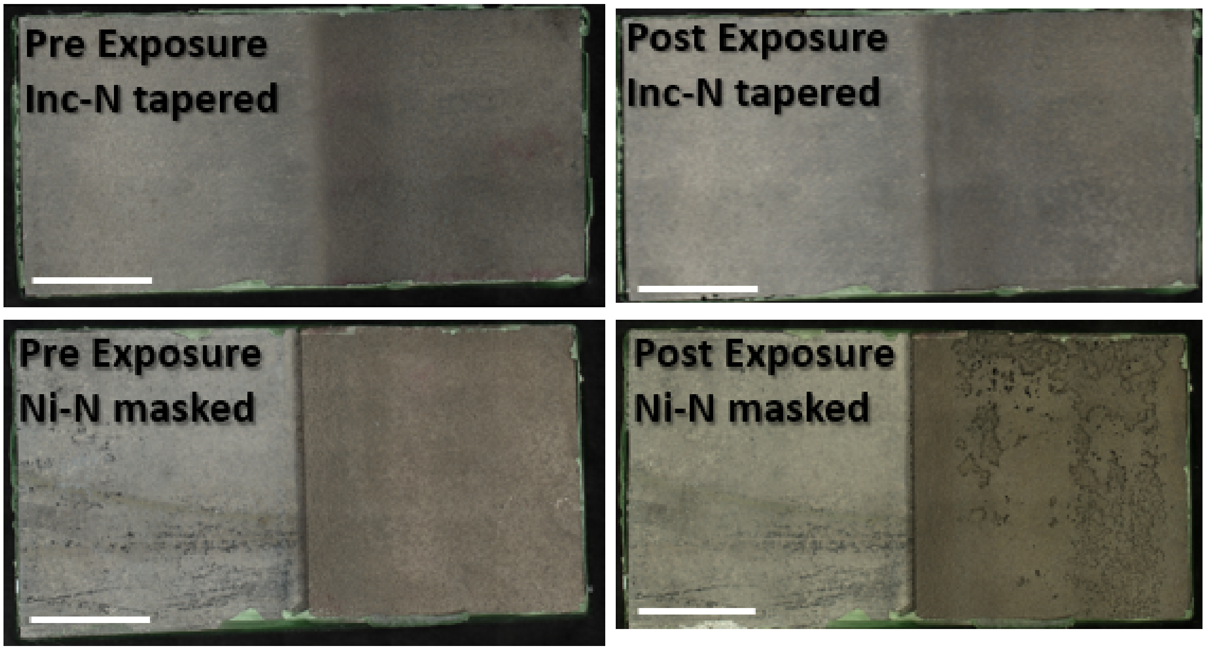

Figure 8: Optical top-down images before and after ferric chloride exposure for Inconel-nitrogen tapered and nickel-nitrogen masked samples. Images are oriented with the substrate on the left and cold spray on the right. Scale bars are all 10 mm.

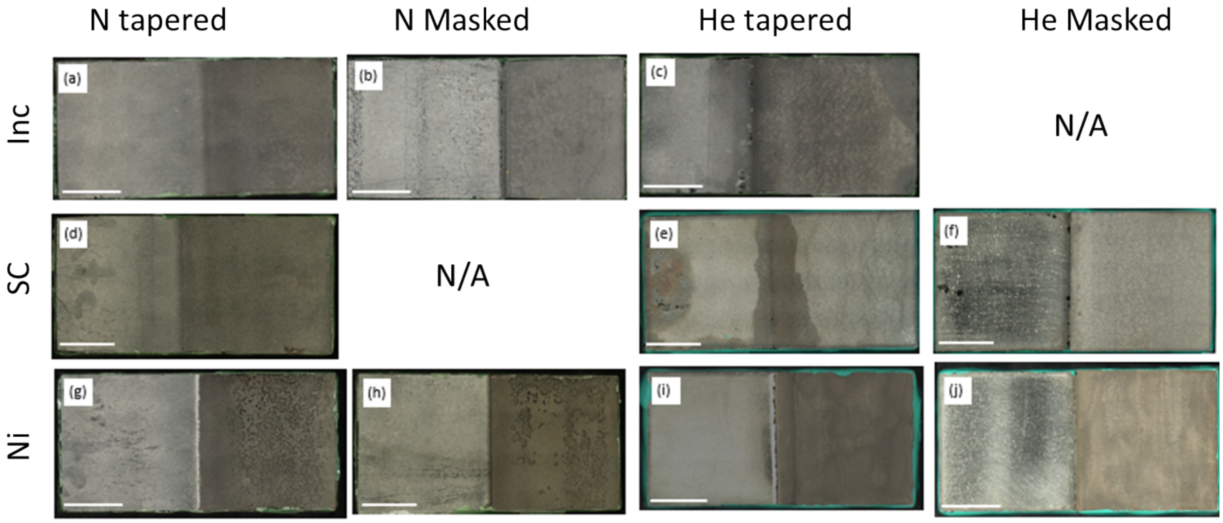

Figure 9: Optical top-down images after ferric chloride exposure of (a) Inconel-nitrogen tapered, (b) Inconel-nitrogen masked, (c) Inconel-helium tapered, (d) Super C-nitrogen tapered, (e) Super C-helium tapered, (f) Super C-helium masked, (g) nickel-nitrogen tapered, (h) nickel-nitrogen masked, (i) nickel-helium tapered, and (j) nickel-helium masked. Images are oriented with the substrate on the left and cold spray on the right. Scale bars are all 10 mm.

For the subset of 316L cold spray samples with CrC particles, pre and post exposure optical images are presented in Figure 10. The post exposure optical images display extensive damage, especially for the NE82-18C and 22 samples. In both cases, it appears that the coating delaminated, and when handled in the lab post-exposure, large pieces of the coatings flaked off. This may be related to the lower carrier gas pressure and flow rate used for these samples. However, in all cases, in the ferric chloride immersion, the cold spray coating behaved poorly with the introduction of hard particles. To fully understand the influence of the introduction of hard particles on subsequent corrosion, samples will need further optimization of the cold spray process and likely characterization under atmospheric environments. Samples sprayed with austenitic stainless steel cold spray (316L and 304L) have not yet been tested, but will be explored in future corrosion testing in the next FY. It should be noted that hard particles were explored here, as they are considered beneficial for enhancing some mechanical properties of the cold spray as well as help to reduce nozzle clogging during deposition. The have been considered a “best practices” for various field portable cold spray applications of high strength alloys[32] however, their applicability in austenitic stainless steels and subsequent effect on the corrosion resistance of these materials relevant for SNF applications warrants further study.

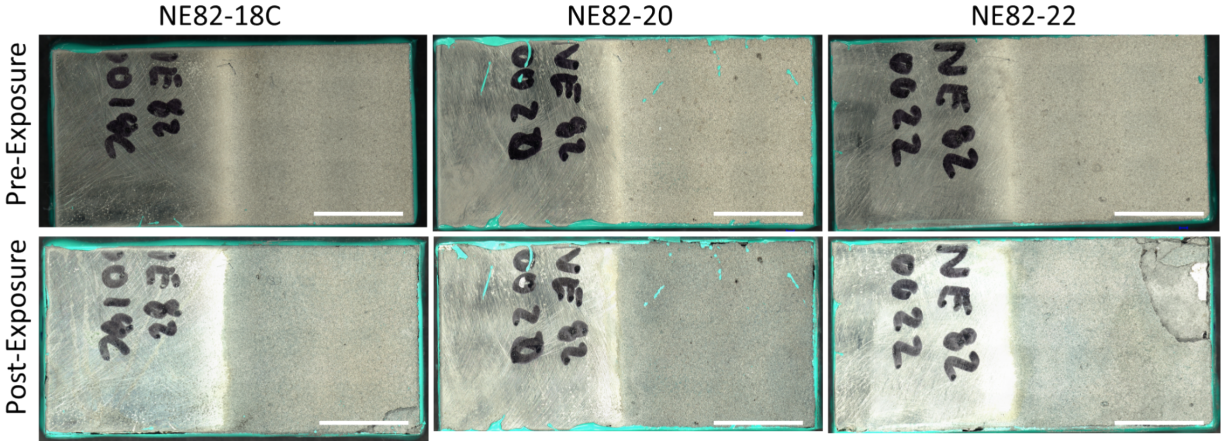

Figure 10. Pre and post $FeCl_3$ exposure optical images for 316L + CrC hard particles.

Higher magnification SEM was used to interrogate the exposed surfaces of the samples. Micrographs from the substrate, at the interface, and in the cold spray were examined for all samples from Figure 9; Figure 11 shows an example from the Inconel-nitrogen tapered sample. Some pitting was observed in the base material (Figure 11-a). Damage was not readily apparently in the cold spray regions in the SEM micrographs and whereas the interfacial regions displayed significant attack, seen in Figure 12.

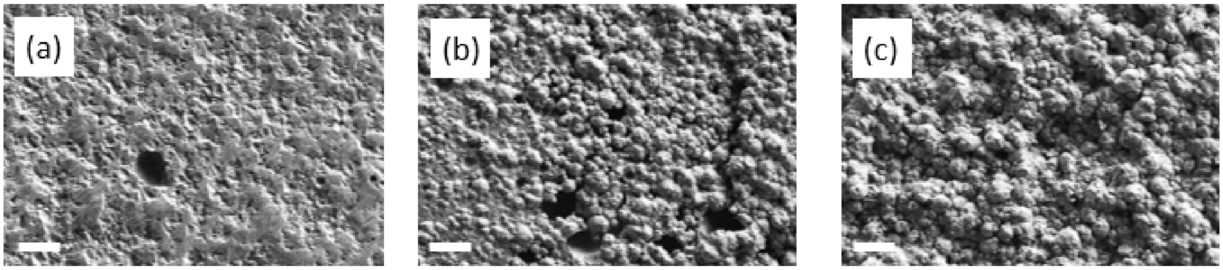

Figure 11: Scanning electron microscopy of Inconel-nitrogen tapered sample after ferric chloride exposure (a) in the substrate, (b) at the interface, with the cold spray oriented on the right and substrate on the left, and (c) in the cold spray. Scale bars are 100 µm.

Evidence of crevicing at the interfaces is somewhat apparent for the tapered edge samples in the micrographs (Figure 12 – a,c,d,e,g,&i). Pits are also observed for all sample types near the junction between cold spray and substrate. Noticeably, for the masked edge samples, pits can occur rather far from the immediate cold spray edge. This could be related to the throwing power of the galvanic couple. The effects of a galvanic couple can be substantial, in some cases occurring inches away from the couple[33]. The diffuse nature of the tapered edge sample makes this more difficult to discern.

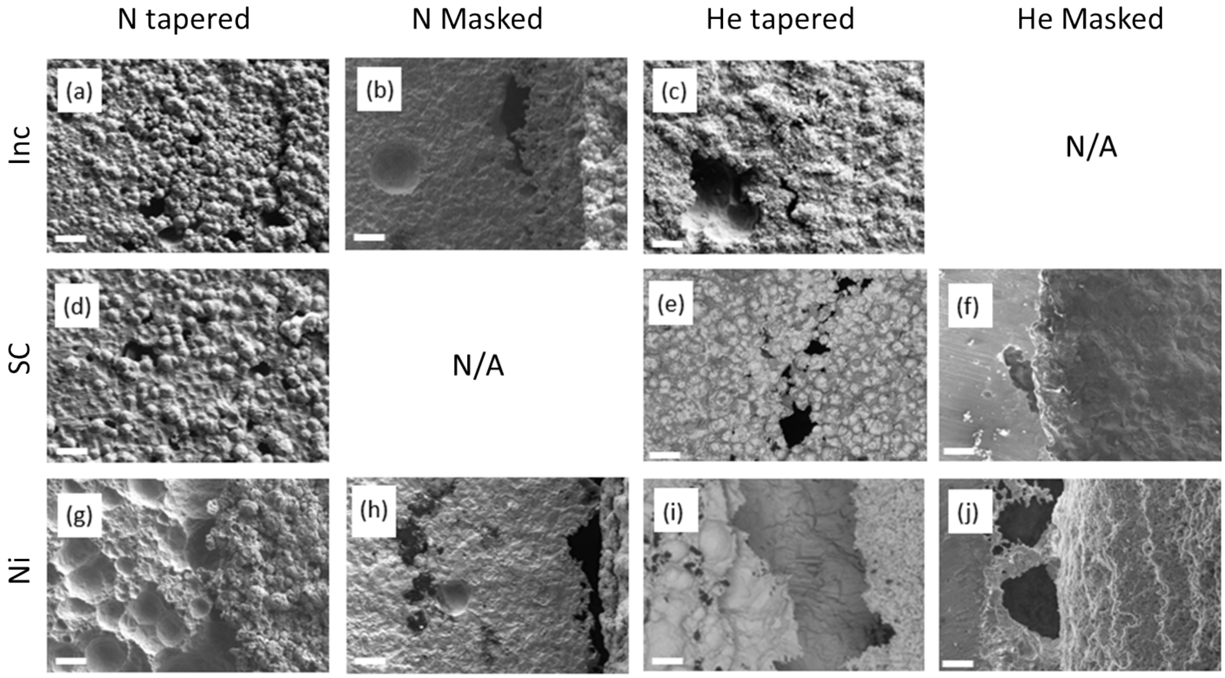

Figure 12: Scanning electron microscopy images at the interface regions after ferric chloride exposure for (a) Inconel-nitrogen tapered, (b) Inconel-nitrogen masked, (c) Inconel-helium tapered, (d) Super C- nitrogen tapered, (e) Super C- helium tapered, (f) Super C-helium masked, (g) nickel-nitrogen tapered, (h) nickel-nitrogen masked, (i) nickel-helium tapered, and (j) nickel-helium masked. Images are oriented with the substrate on the left and cold spray on the right. Scale bars are all 100 µm.

In cross-section, Figure 13, the corrosion attack formed beneath the cold spray becomes much more apparent for all samples. As noted above, the depth and extent of attack in the helium-processed Super C and nickel samples should not be directly compared to the other samples due to the difference in ferric chloride hydration and potentially in concentration. However, for both exposure sets of samples, regardless of edge type, the porosity appears to dictate whether damage forming at the interface will occur in both the substrate and cold spray or just in the substrate. The samples with porosity greater than approximately 5% sustained noticeable damage in the cold spray as well as the substrate. The lower porosity samples, however, appear to have the damage focused in the substrate materials.

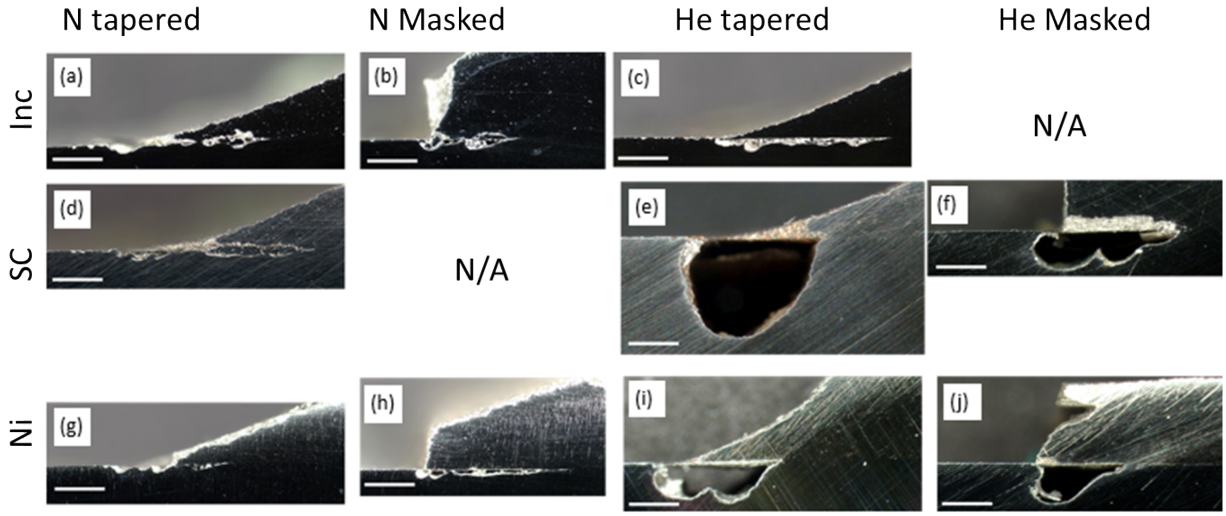

Figure 13: Optical microscopy of cross sections, after ferric chloride exposure (a) Inconel-nitrogen tapered, (b) Inconel-nitrogen masked, (c) Inconel-helium tapered, (d) Super C- nitrogen tapered, (e) Super C- helium tapered, (f) Super C-helium masked, (g) nickel-nitrogen tapered, (h) nickel-nitrogen masked, (i) nickel-helium tapered, and (j) nickel-helium masked. Images are oriented with the patch on the upper right. The substrate occupies the lower portion of the image. Scale bars are all 1 mm.

3.2.3 Metallurgical evaluation – full immersion pitting exposures

To further examine potential effects of the underlying microstructure, and possible changes enhanced by the cold spray process itself, phase maps and electron backscatter detection (EBSD) were employed on the post-exposure cross-sections. Two regions were examined for comparison; the interface between the cold spray and base material far from the patch edge (unaffected by the corrosion exposure) and at the patch edge, where corrosion had occurred. Body-centered cubic (BCC) phase martensite can form in 304 stainless steel, which is primarily face-centered cubic (FCC) austenite, under large enough strain. The BCC martensite will have a faster dissolution rate than the FCC austenite, and thus would be more readily attacked. As cold spray requires high kinetic energy levels to deform the metal particles, EBSD was applied to examine the near surface region for BCC phase material, to explore potential stress-induced phase changes and/or the high strains present in the underlying substrate.

Figure 14-a-c displays an interface region far from the patch edge for the Inconel-nitrogen masked sample (the cold spray is oriented to the top of all the images and is often seen as black as no diffraction patterns were picked up from the highly deformed particles at the resolutions examined). When comparing the forward scatter detector image, Figure 14-a, to the phase map and EBSD, Figure 14-b&c, it becomes apparent that the material closest to the interface (above and below), within approximately 5 µm, does not give clear diffraction patterns, leading to a black, "missing" region in the phase map and EBSD. Therefore, statements cannot be made about the BCC content in this region. The corrosion damage at the interface, however, extends substantially beyond this and in the visible near surface region in the 304L substrate, no concentration of BCC phase is seen. The distribution of the BCC phase seen in the region far from the patch edge is consistent with the bulk material, more easily seen in Figure 14(f). The EBSD far from the patch edge, Figure 14-c, does reveal a layer of deformation appearing as a watercolor-like pattern in the phase image, extending approximately 20 µm into the substrate. This layer is, again, much thinner than that of the corrosion damage. At the corrosion front, however, the corroded area is much narrower, similar in magnitude to the deformation layer.

This trend continued across all samples evaluated with EBSD. No substantial differences in the deformation layer or phase map were found between edge type or processing gas. Figure 15 shows the results for Inconel-nitrogen tapered and Figure 16 shows the results for the Inconel-helium tapered. Deformed 304L stainless steel, even if it has not undergone a phase transformation to BCC martensite, will experience higher dissolution rates than that of the relaxed FCC austenite. Therefore, the deformed layer in the 304L substrate material is likely advancing, but not the sole contributor to, the corrosion front.

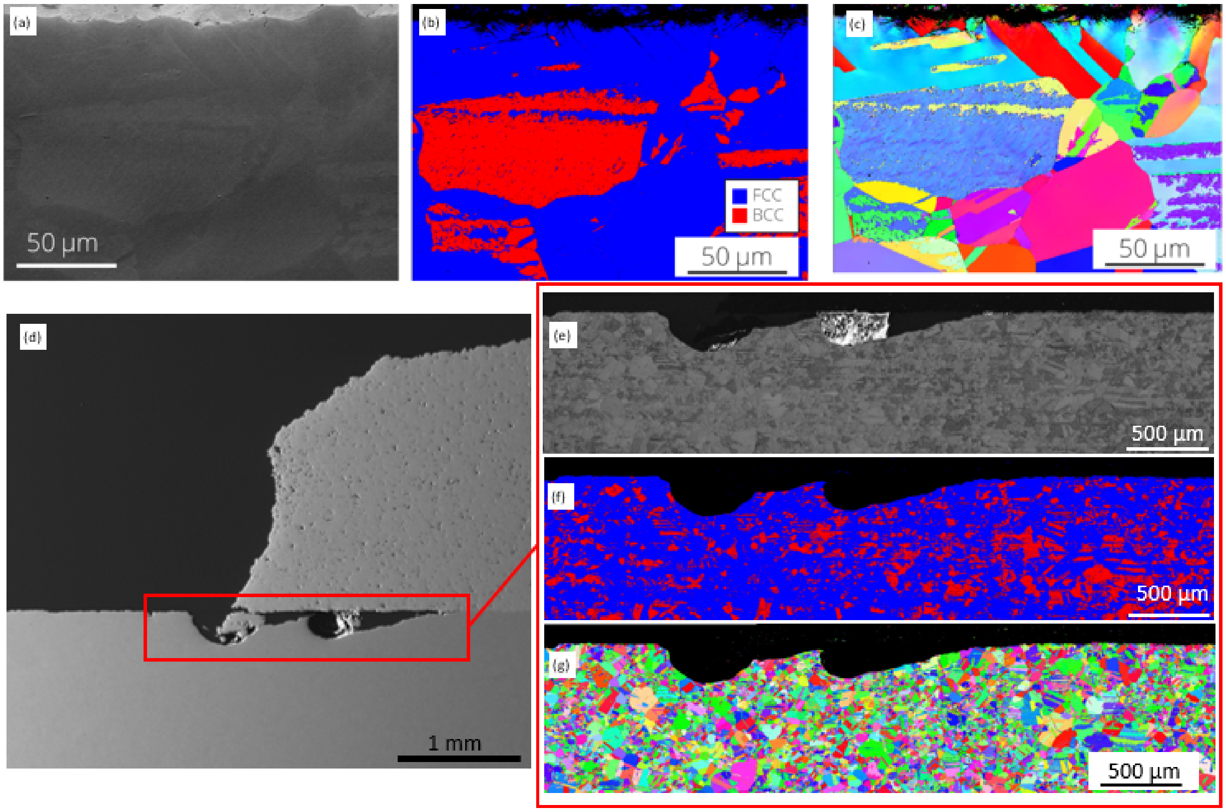

Figure 14: (a) Forward scatter detector micrograph, (b) phase map, and (c) EBSD inverse pole figure (displaying crystal orientation in the x direction) for the Inconel-nitrogen masked sample, far from the patch edge. Also shown is (d) scanning electron microscopy at the patch edge and the corresponding (e) band contrast, (f) phase map, and (g) electron backscatter diffraction.

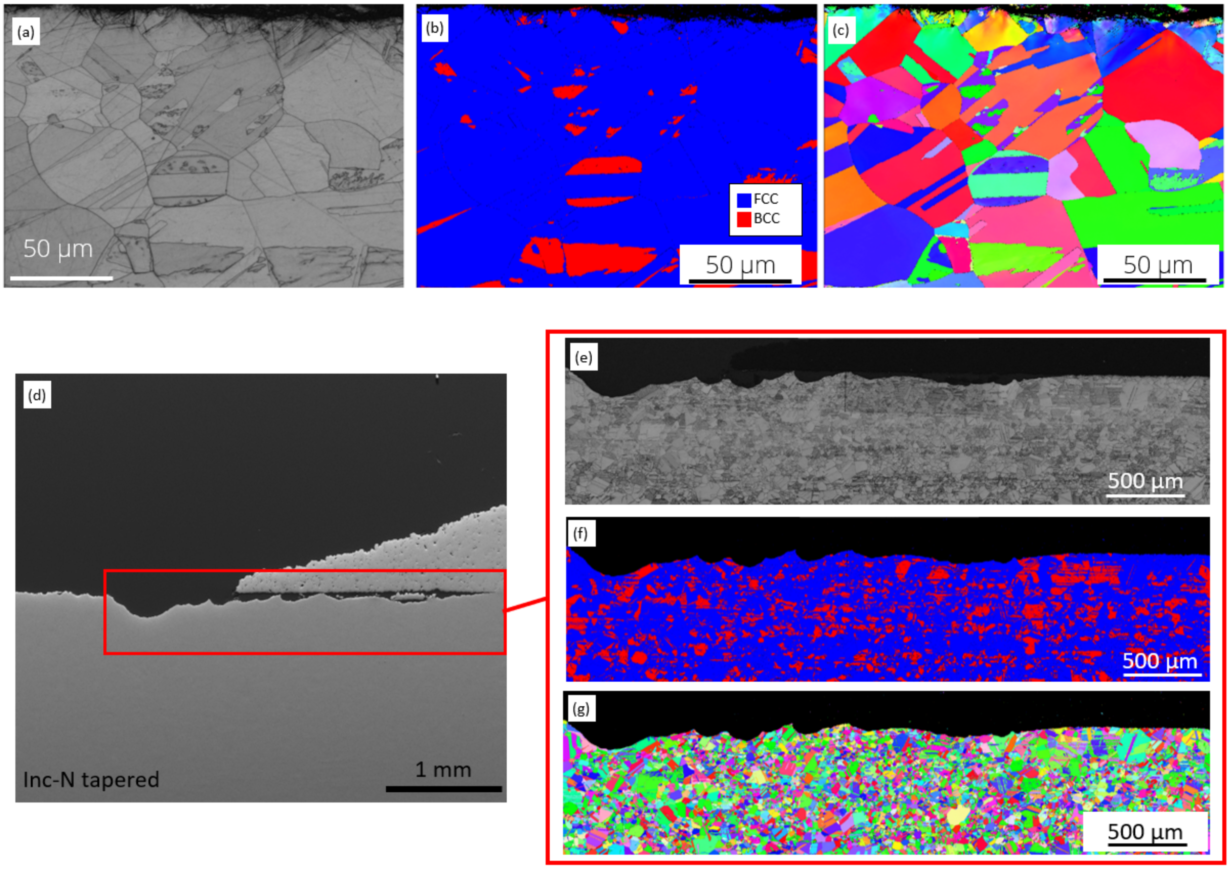

Figure 15: (a) Band contrast, (b) phase map, and (c) EBSD inverse pole figure (displaying crystal orientation in the x direction) in the substrate far from the patch edge for the Inconel-nitrogen tapered sample after ferric chloride exposure. Also shown is (d) scanning electron microscopy at the patch edge and the corresponding (e) band contrast, (f) phase map, and (g) electron backscatter diffraction.

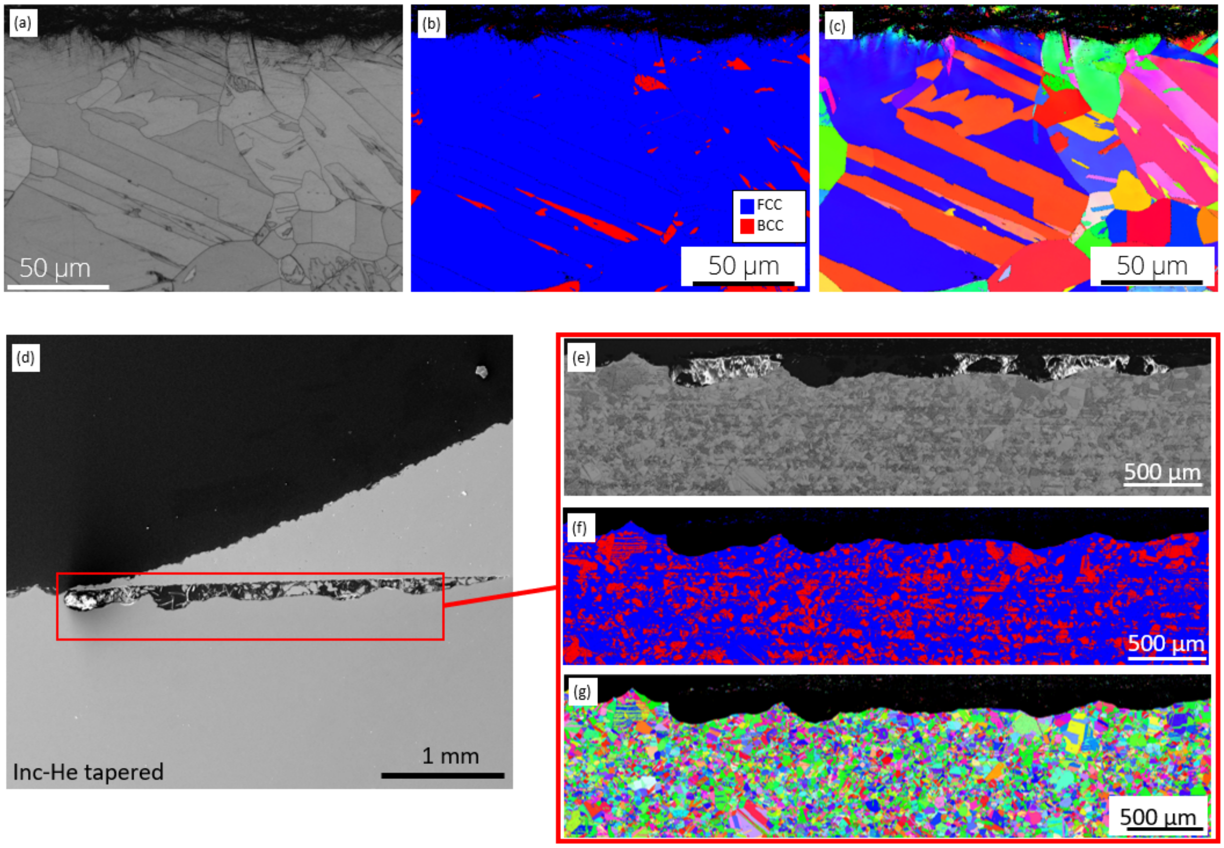

Figure 16: (a) Band contrast, (b) phase map, and (c) EBSD inverse pole figure (displaying crystal orientation in the x direction) in the substrate far from the patch edge for the Inconel-helium tapered sample after ferric chloride exposure. Also shown is (d) scanning electron microscopy at the patch edge and the corresponding (e) band contrast, (f) phase map, and (g) electron backscatter diffraction

Nanoindentation results are shown in Figure 17 for the nickel-nitrogen tapered sample. Indents were collected from 1 mm above the interface in the cold spray material and down across the interface to roughly 0.75 mm into the substrate material. Preliminary data has been collected and further data analysis is in progress. In this instance, a lower hardness is observed in the Ni cold spray coating than in the 304L base material.

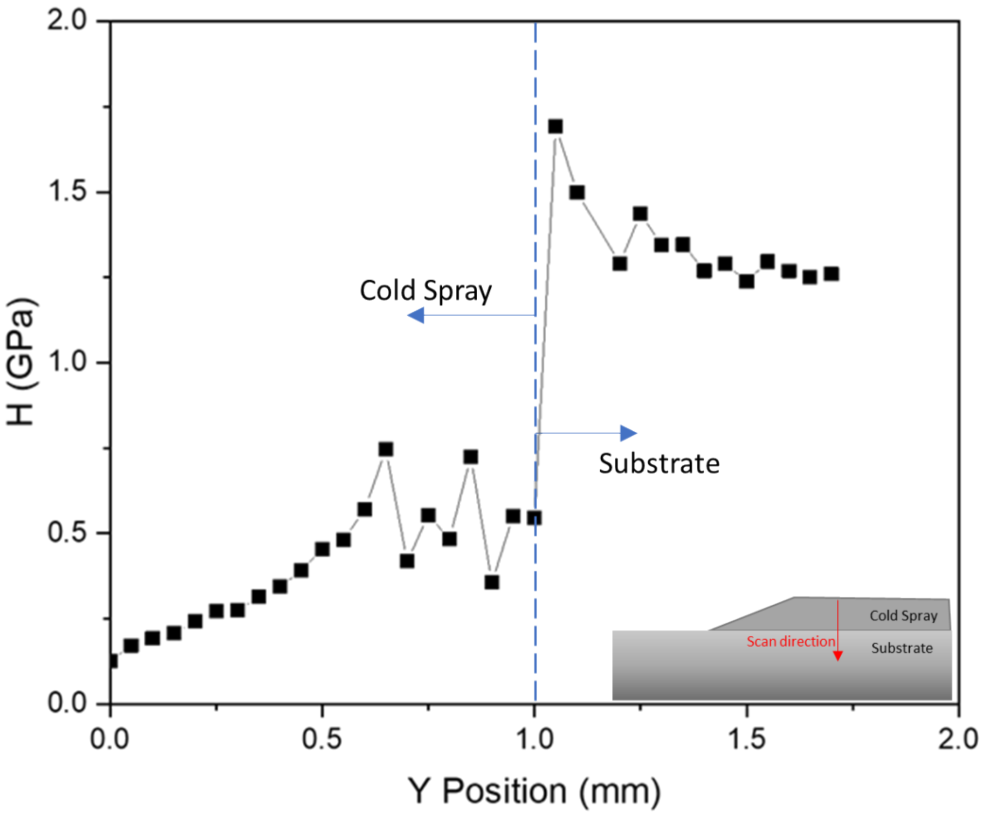

Figure 17: Hardness values going from 1 mm above the interface in the cold spray to 0.75 mm into the 304L substrate material on the nickel-nitrogen tapered sample.

3.2.4 Atmospheric Exposures

Optical top-down images were collected before and after atmospheric exposures. Figure 18 contains an exemplar set from the Super C-nitrogen tapered sample exposed to 75% RH and 35 °C for 8 weeks. Some pink staining can be seen in the cold spray region. Near the patch edge, the post exposure image shows signs of pitting and dark corrosion product. In Figure 19 and Figure 18, higher magnification optical images at the patch edge are shown for a selection of samples exposed at the three different conditions (constant RH and cyclic conditions).

Figure 18: Pre and post exposures for Super C-nitrogen tapered exposed to 75% RH and 35 °C. Scale bars are 5 mm. Cold spray is oriented towards the top of the image, substrate towards the bottom.

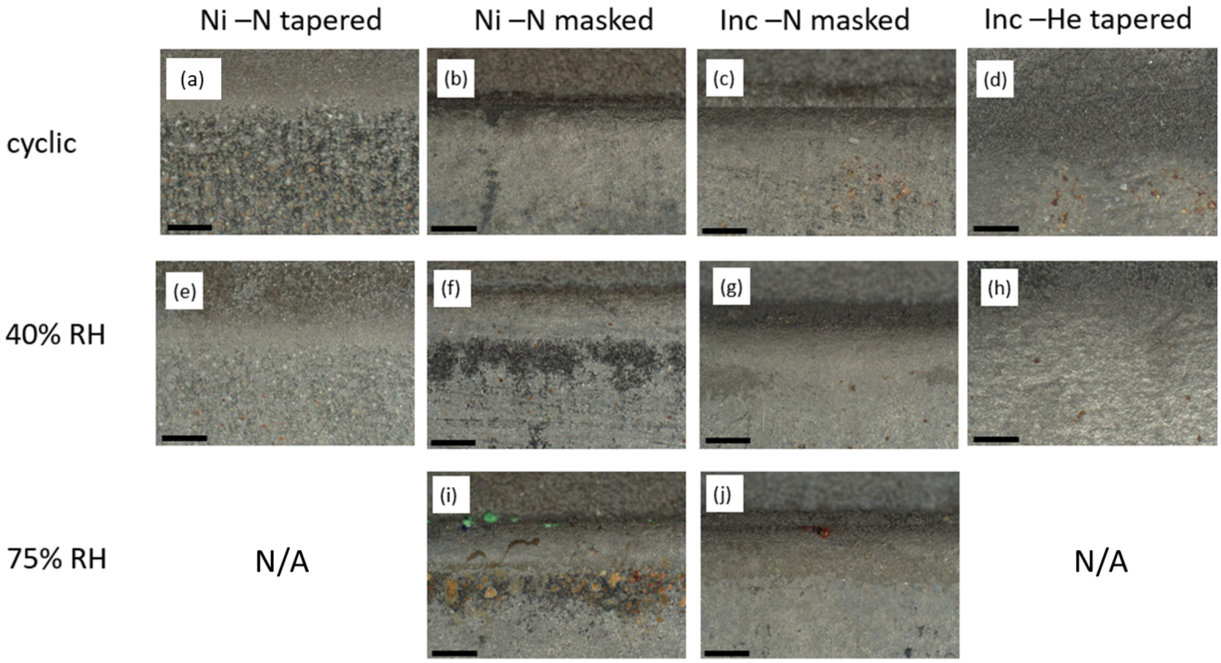

Figure 19: Post 8 week atmospheric exposure optical images in the interface regions for (a) (e) nickel-nitrogen tapered, (b) (f) (i) nickel-nitrogen masked, (c) (g) (j) Inconel-nitrogen masked, and (d) (h) Inconel-helium tapered under (a)-(d) cyclic conditions, (e)-(h) 40% RH 35 °C, and (i) (j) 75% RH 35 °C. Images are oriented with the cold spray at the top of the image and the substrate towards the bottom. Scale bars are 1 mm.

While some damage can be observed at the interface through optical imaging, it is not entirely clear the extent of the damage. Further SEM micrographs were obtained to better determine the post-exposure corrosion damage. Figure 20 displays the interface region for the Inc, Ni, and SC cold spray samples exposed at 75% RH for 10 weeks. It can be observed, especially in the BSE images, that significant amounts of corrosion product (darker shades in BSE) built up near the interface for both samples. In the Inc and Ni masked sample cases, the corrosion product appears to occur right at the interface and again accumulates at a distance from the interface. The tapered sample displays that corrosion damage occurs throughout the tapered region all along the interface. These attack morphologies (as observed from the top-down images) are similar in form to the corrosion damage observed in the previous full immersion ferric chloride pitting tests, indicating that the $FeCl_3$ exposures are likely a representative accelerated corrosion test, which will be useful to help optimize cold spray properties for atmospheric conditions. Additionally, Figure 21 displays the cold spray regions of the same samples post-exposure. Corrosion product can be observed to accumulate between the cold spray particles on the surface. In FY23, samples are planned to be cross-sectioned and re-imaged for further analysis to determine if damage occurred underneath the cold spray at the interface and the extent of the potential underlying corrosion attack that cannot be observed from the top-down images alone.

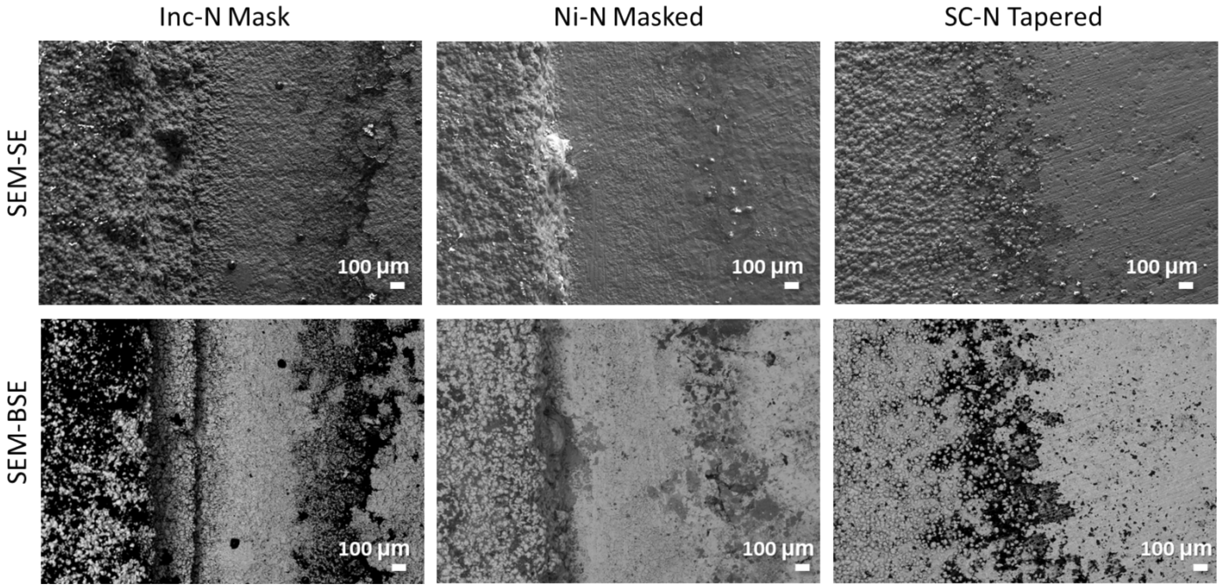

Figure 20. Post-exposure images for the interfaces of coupons exposed in 75% RH for 10 weeks displaying buildup of corrosion products at and near the interface. Secondary electron (SE) images in top row with corresponding back scattered electron (BSE) images in bottom row. Cold spray is oriented to the left of the images and base material to the right.

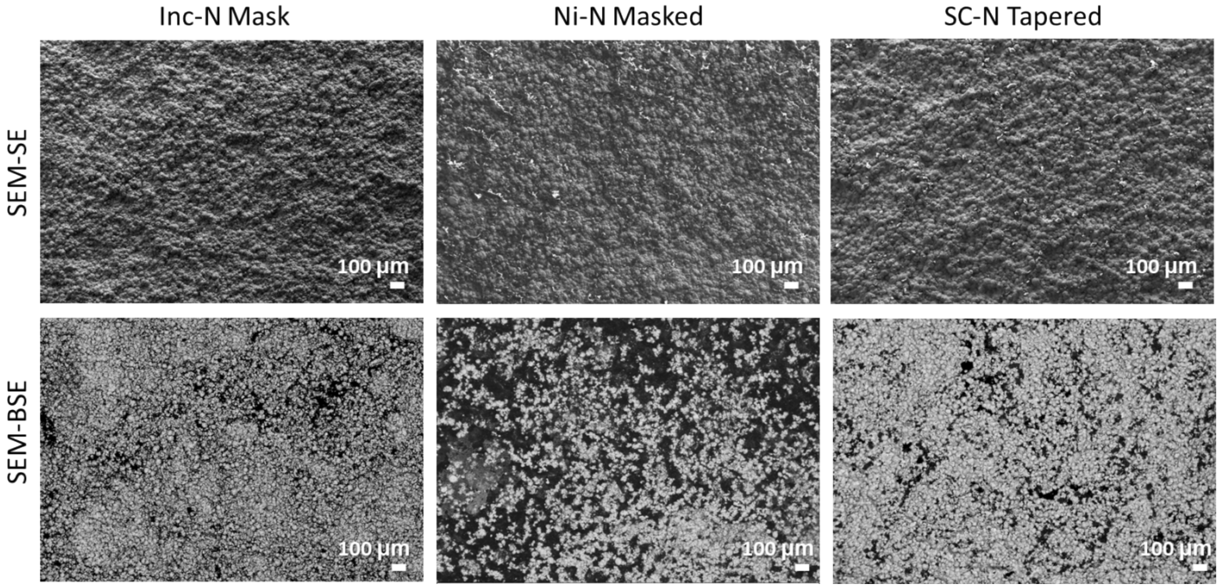

Figure 21. Post-exposure images for the cold spray region of coupons exposed in 75% RH for 10 weeks displaying buildup of the corrosion products between the cold spray particles. Secondary electron (SE) images in top row with corresponding back scattered electron (BSE) images in bottom row.

Additional samples were exposed at a lower RH conditions, 40%, and results of the 10 week exposures are provided in Figure 22 and Figure 23. Again, in the 40% RH conditions, which would have much lower volumes of electrolyte coverage on the surface, similar corrosion attack morphologies are observed for both the tapered and masked interfaces. These are also consistent with those previously observed in $FeCl_3$ solutions.

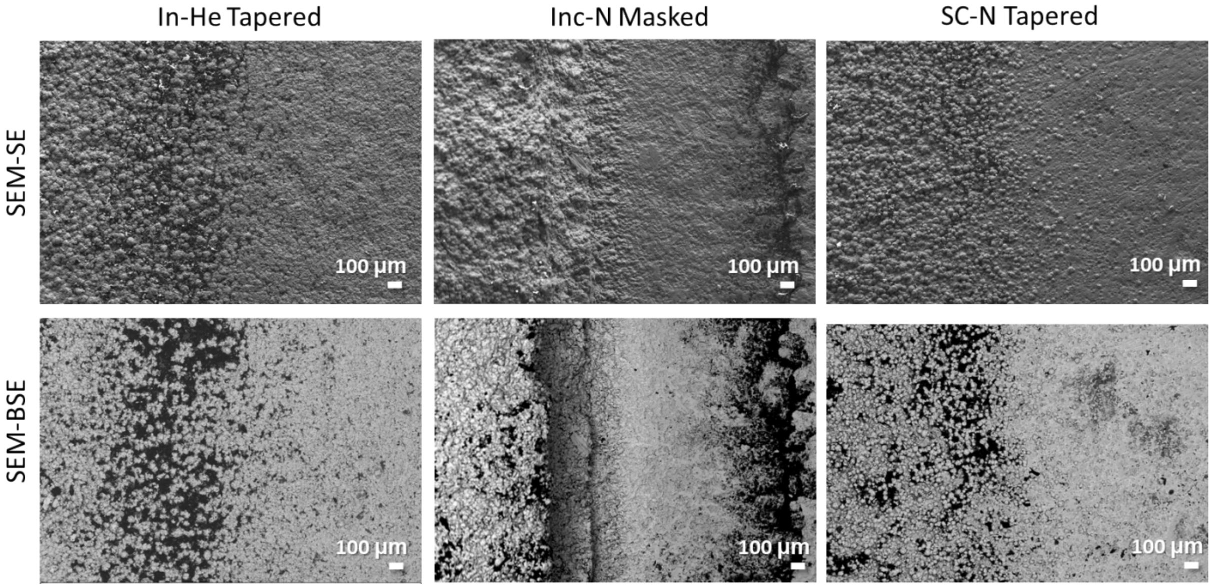

Figure 22. Post-exposure images for the interfaces of Inc and SC coupons exposed in 40% RH for 10 weeks displaying buildup of corrosion products at and near the interface. Secondary electron (SE) images in top row with corresponding back scattered electron (BSE) images in bottom row. Cold spray is oriented to the left of the images and base material to the right.

Additional images of the cold spray regions of the samples post 10 week exposure are presented in Figure 24 and Figure 25. Again, corrosion attack can be observed across all cold spray samples, with the most severe attack observed on the Ni coating. This is also consistent with previous data obtained from the accelerated testing in both NaCl potentiodynamic polarizations and $FeCl_3$ full immersion exposures.

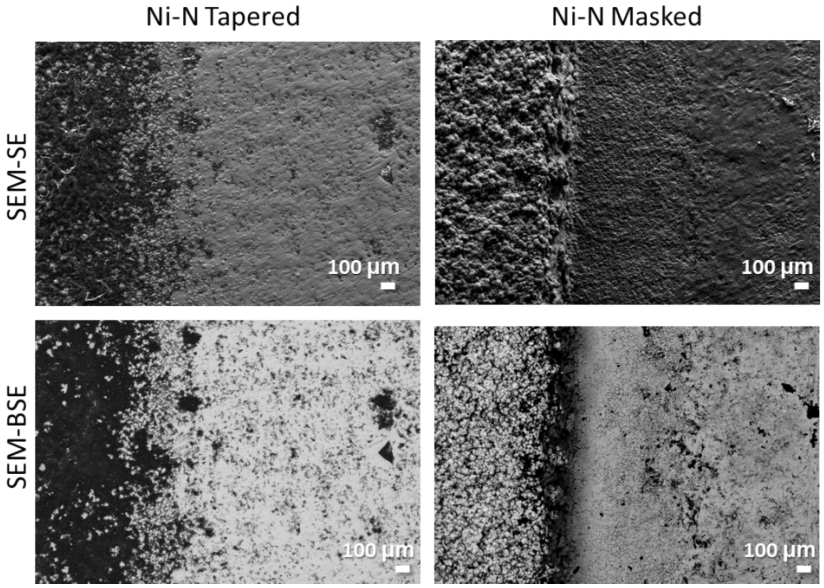

Figure 23. Post-exposure images for the interfaces of Ni coupons exposed in 40% RH for 10 weeks displaying buildup of corrosion products at and near the interface. Secondary electron (SE) images in top row with corresponding back scattered electron (BSE) images in bottom row. Cold spray is oriented to the left of the images and base material to the right.

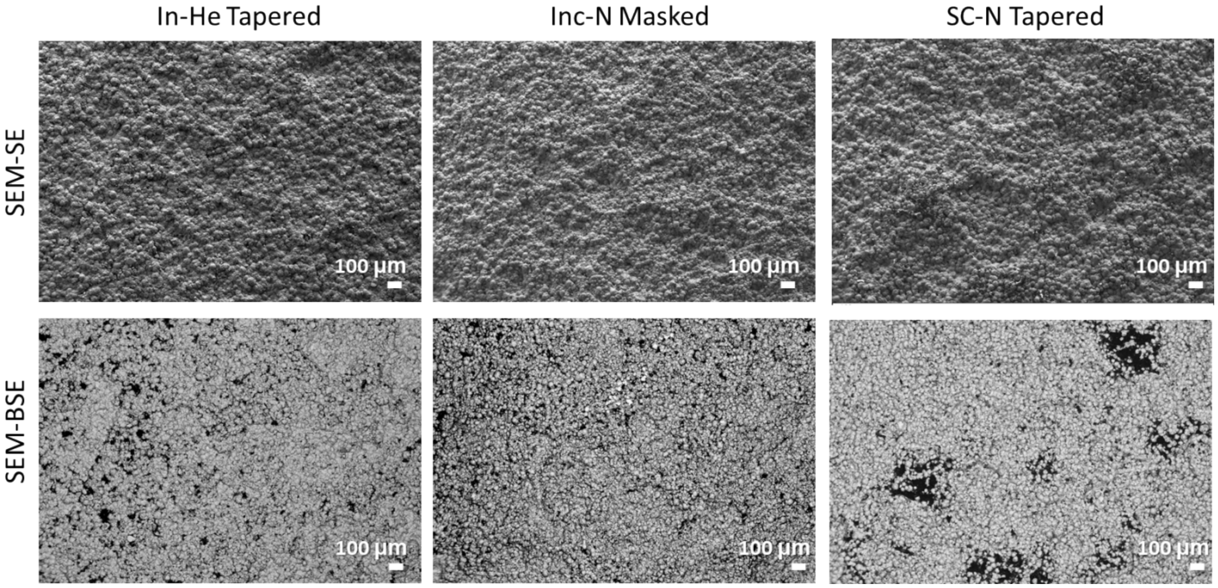

Figure 24. Post-exposure images for the cold spray regions of Inc and SC coupons exposed in 40% RH for 10 weeks displaying buildup of the corrosion products between the cold spray particles. Secondary electron (SE) images in top row with corresponding back scattered electron (BSE) images in bottom row.

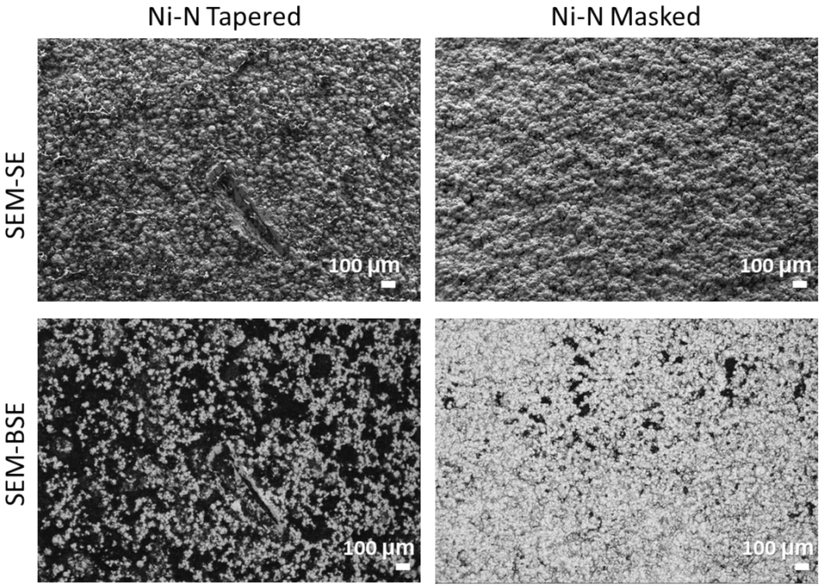

Figure 25. Post-exposure images for the cold spray regions of Ni coupons exposed in 40% RH for 10 weeks, secondary electron (SE) images in top row with corresponding back scattered electron (BSE) images in bottom row.

These samples will be further evaluated in FY23 using SEM and cross-sectional analysis. The initial results of the atmospheric exposure samples highlight that attack is still observed at the cold spray/base material interface under more relevant atmospheric exposure conditions for SNF canisters. Additionally, the morphology of attack and the severity of attack is consistent with trends observed from previous accelerated testing, indicating that these accelerated tests are good tools for optimization of cold spray coatings for use under atmospheric exposure conditions. However, the extent of the potential underlying attack and whether this forms under atmospheric conditions still needs further investigation, and, will be a focus of early FY23 studies.

3.2.5 Accelerated testing – boiling $MgCl_2$ for SCC evaluation

In FY22, a subset of the cold spray coupons were exposed in boiling $MgCl_2$ solution for one week. While coupons were exposed without applying an external stress, the objective was to determine if the cold spray deposition process itself induced significant strain at the patch edges (to counterbalance the compressive stress beneath the patches) that might potentially reduce the resistance to SCC. Optical images were taken of the interface regions post exposure and are provided in Figure 26. While significant corrosion damage is observed, no visual signs of cracking at the interface were observed. However, further investigation with SEM and cross-sectional analysis are planned to be carried out in FY23 to fully determine the extent of the damage. Additional plans may also include larger sample sets (when coupons are available) and sets of cold spray on stressed samples to better mimic weld regions and weld residual stresses.

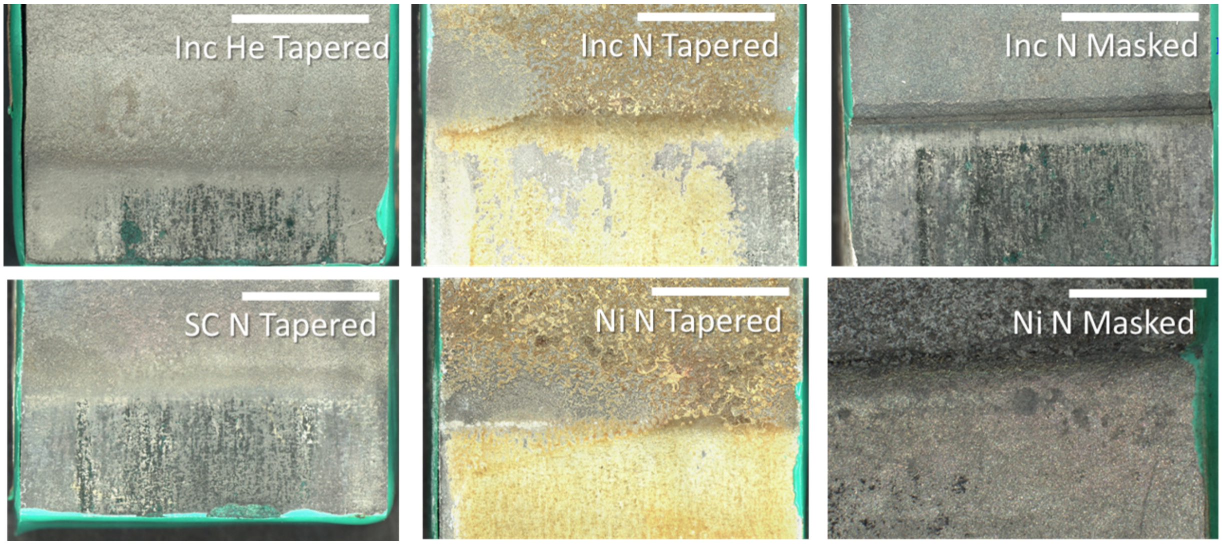

Figure 26. Optical images of interface regions post-boiling $MgCl_2$ exposures for one week. Samples display corrosion attack, but no SCC indication visibly (note samples were not stressed during exposure, only residual stresses due to CS are present). Scale bars are 10 mm for all.

4. Conclusions

High pressure cold spray is considered a leading technology as a barrier coating for mitigation and repair of SNF dry storage canisters. Cold spray has been shown to be a promising technique as a corrosion barrier in various applications yet needs further evaluation in canister relevant conditions. The work presented herein was a preliminary analysis to help understand the corrosion behavior of cold spray to aid in its optimization as a coating barrier for relevant environments.

Consistent with learnings in FY21, full immersion accelerated electrochemical testing continued to indicate that the surface roughness of the cold spray material plays a role in its susceptibility to metastable pitting; grinding the surface improved the resistance to metastable pitting. Additionally, the role of the dissimilar metals at the interface was further explored in FY22. This was observed in FeCl3 accelerated pitting testing where all interfaces of the samples examined presented the most deleterious regions for corrosion. In tapered samples, pitting was exacerbated in regions where the cold spray did not form fully dense layers. In the masked samples, two modes of corrosion were observed; enhanced attack at the boundary between the base material and cold spray, and enhanced pitting zones in the near-interface regions. Cross-sectioning of the exposed samples displayed that the attack at the interface extended beneath the cold spray patches in all cases for the accelerated $FeCl_3$ immersion exposure. In samples with greater porosity in the cold spray coating, the attack was observed to extend into the cold spray itself. However, when porosity was reduced, the attack was confined to the substrate. Additional metallography was carried out on these cross-sections and a region of deformation of the substrate was observed near the interfaces. It is believed that the underlying attack initiates in this highly deformed layer and then continues further with expanded growth near the mouth due to the crevice formed and the galvanic conditions present. However, this still warrants further analysis under relevant atmospheric conditions to establish if underlying attack will also occur in these. Also, in FY22, a subset of the electrochemical tests consisting of full immersion $FeCl_3$ exposures was carried out on cold spray coatings containing CrC hard particles. These coatings with CrC hard particles displayed enhanced corrosion attack and in their current state, are not likely good candidates for use under atmospheric corrosion conditions. It is not fully clear whether the mechanism behind the increased corrosion attack of the cold spray is due to galvanic effects between the cold spray and hard particles or if it is due to increased porosity from the nitrogen carrier gas.

In FY22, relevant atmospheric exposures were carried out for times of up to 10 weeks exposure. Both optical and SEM imaging indicated enhanced attack at the cold spray/base material interface under all atmospheric exposure conditions. Additionally, the morphology of attack for both the masked and tapered samples from the top-down images displayed the same form as the morphology of attack in the full immersion accelerated tests. Finally, materials that displayed higher susceptibility in full immersion (Ni cold spray) also showed enhanced corrosion under atmospheric testing. While further cross-sectional analysis is necessary to determine the full extent of attack at the interface and the potential subsurface attack, these studies indicate that the selected accelerated corrosion tests are applicable tools for optimization of cold spray coating for use under marine atmospheric exposure conditions.

Finally, in FY22, initial exposures were carried out in boiling $MgCl_2$ solutions to evaluate the potential effects of the cold spray process itself on SCC resistance. Initial optical images indicated that corrosion attack occurred, but did not indicate enhanced SCC susceptibility.

Overall FY22 results displayed good correlation between the selected accelerated corrosion tests and observations from more relevant atmospheric exposure testing. Further examination, including cross-sectional analysis, is necessary to fully understand the corrosion extent and damage under the atmospheric conditions for full comparison to the accelerated tests. Geometric effects and residual stresses are other factors of interest at the interface. Future testing will include more rigorous corrosion evaluation of optimized cold spray samples, in terms of both materials and geometries, in SNF canister-relevant environments.

Thus far, from both accelerated and relevant atmospheric examinations of cold spray samples, three main factors have been determined to influence corrosion and could benefit most from process optimization; cold spray porosity, cold spray material selection, and interface geometry. With regards to porosity, lowered porosity of the cold spray led to reduced the attack of the cold spray layer itself. Thus, optimization of spray processes to reduce porosity may enhance cold spray as a protective coating. Material selection, specifically materials that were closer in composition and corrosion potential to the base material, showed less influence of galvanic attack. Ni, which is farther from 304L stainless steel than the other tested cold spray materials showed the highest signs of attack. Optimizing material selection to reduce galvanic potentials may enhance overall protection capabilities. Finally, the interface morphology itself led to different modes of attack, with tapered interfaces spreading the damage and masked interfaces concentrating it further near the interface. It has not been determined which is better yet for overall protection, but further optimization of the morphology may help reduce the long-term attack. Optimization of coatings with respect to all three of these properties and analysis of the subsequent corrosion performance of the coatings will be the focus of work to be carried out in future FYs.

5. References

1. Knight, A.W.N., B.L.; Bryan, C.R.; Schaller, R.F., *FY21 Status Report: SNF Canister Coatings for Corrosion Prevention and Mitigation*, U.S.D.o. Energy, Editor. 2021.
2. Bryan, C.R.K., A.W.; Nation, B.L.; Montoya, T.; Karasz, E.; Katona, R.; Schaller, R.F., *FY21 Status Report: SNF Interim Storage Canister Corrosion and Surface Environment Investigations*, U.S.D.o. Energy, Editor. 2021.
3. Schaller, R.F., et al., *FY20 Status Report: SNF Interim Storage Canister Corrosion and Surface Environment Investigations*. 2020, Sandia National Laboratories: Albuquerque, NM.
4. Ross, K.A., et al., *Investigation of Cold Spray as a Dry Storage Canister Repair and Mitigation Tool*. 2020, Pacific Northwest National Laboratories: Richland, WA. p. 70.
5. Ross, K.A., et al., *Assessment of Cold Spray Technology for Nuclear Power Applications*. 2021, U.S. Nuclear Regulatory Commission: Washington, D.C.
6. Smith, M.F., *Introduction to Cold Spray*, in *High Pressure Cold Spray-Principles and Applications*, C.M. Kay and J. Karthikeyan, Editors. 2016, ASM International.
7. Champagne, V.K. and D.J. Helfritch, *Mainstreaming cold spray – push for applications.* Surface Engineering, 2014. **30**(6): p. 396-403.
8. Papyrin, A., *Cold Spray Technology.* Advanced Materials & processes, 2001. **159**(9).
9. Wu, K., et al., *An investigation into microstructure, tribological and mechanical properties of cold sprayed Inconel 625 coatings.* Surface and Coatings Technology, 2021. **424**.
10. Wang, H.-T., et al., *Cold spraying of Fe/Al powder mixture: Coating characteristics and influence of heat treatment on the phase structure.* Applied Surface Science, 2008. **255**(5): p. 2538-2544.
11. Toribio, J., *Residual Stress Effects in Stress-Corrosion Cracking.* Journal of Materials Engineering and Performance, 1998. **7**: p. 173-182.
12. Luzin, V., et al., *Advanced Residual Stress Analysis in Thermal Spray and Cold Spray Processes.* Journal of Thermal Spray Technology, 2020. **29**(6): p. 1211-1217.
13. Vilardell, A.M., et al., *Cold spray as an emerging technology for biocompatible and antibacterial coatings: state of art.* Journal of Materials Science, 2015. **50**(13): p. 4441-4462.
14. Leyman, P.F. and V.K. Champagne, *Cold Spray Process Development for the Reclamation of the Apache Helicopter Mast Support*. 2009.
15. Yeom, H. and K. Sridharan, *Cold spray technology in nuclear energy applications: A review of recent advances.* Annals of Nuclear Energy, 2021. **150**.
16. Nardi, A.C.V.F., G.; Nault, I.; Story, W.; Nikolov, D. , *Chrome Replacement and Recent Advancements*, in *In Cold Spray Action Team Meeting*. 2019: https://55922c16-bbf4-4650-aa4d-6d5bfb8c7a14.filesusr.com/ugd/0ebd9c_638d644acea54db3b7695142978f938a.pdf.
17. Schaller, R.F., et al., *Corrosion Properties of Powder Bed Fusion Additively Manufactured 17-4 PH Stainless Steel.* Corrosion, 2017. **73**(7): p. 796-807.
18. Bala, N., et al., *Cold spray coating process for corrosion protection: a review.* Surface Engineering, 2013. **30**(6): p. 414-421.
19. Hassani-Gangaraj, S.M., A. Moridi, and M. Guagliano, *Critical review of corrosion protection by cold spray coatings.* Surface Engineering, 2015. **31**(11): p. 803-815.
20. Champagne, V.K., V.K. Champagne, and C. Widener, *Cold Spray Applications*, in *Cold-Spray Coatings*. 2018. p. 25-56.
21. Rokni, M.R., et al., *Review of Relationship Between Particle Deformation, Coating Microstructure, and Properties in High-Pressure Cold Spray.* Journal of Thermal Spray Technology, 2017. **26**(6): p. 1308-1355.
22. Gwalani, B., Miao Song, Joshua Silverstein, Julian Escobar, Tianhao Wang, Mayur Pole, Kyle Johnson, Bharat K. Jasthi, Arun Devaraj, and Kenneth Ross, *Thermal stability and mechanical properties of cold-sprayed Nickel-Yttria coating.* Scripta Materialia, 2022. **207**.
23. Jiang, X., Overman, N., Smith, C., & Ross, K., *Microstructure, hardness and cavitation erosion resistance of different cold spray coatings on stainless steel 316 for hydropower applications.* Materials Today Communications, 2020. **25**.
24. Sample, C.M., et al., *Factors governing static properties and fatigue, fatigue crack growth, and fracture mechanisms in cold spray alloys and coatings/repairs: A review.* Additive Manufacturing, 2020. **36**.
25. Karasz, E., et al., *Measuring the residual stress and stress-corrosion cracking susceptibility of additively manufactured 316L by ASTM G36-94.* Corrosion, 2021.

26. Ross, K.A., et al., *In Preparation: Cold Spray for Mitigation and Repair of Spent Nuclear Fuel Dry Storage Canisters* 2021, Pacific Northwest National Laboratories.
27. International, A., *Standard Test Methods for Determining Area Percentage Porosity in Thermal Sprayed Coatings*. 2021.
28. Schneider, C.A., W.S. Rasband, and K.W. Eliceiri, *NIH Image to ImageJ: 25 years of image analysis.* Nat Methods, 2012. **9**(7): p. 671-5.
29. International, A., *Standard Test Methods for Pitting and Crevice Corrosion Resistance of Stainless Steels and Related Alloys by Use of Ferric Chloride Solution*. 2015.
30. International, A., *Standard Practice for Evaluating Stress-Corrosion-Cracking Resistance of Metals and Alloys in a Boiling Magnesium Chloride Solution*. 2013.
31. Weirich, T.D., et al., *Humidity Effects on Pitting of Ground Stainless Steel Exposed to Sea Salt Particles.* Journal of The Electrochemical Society, 2019. **166**(11): p. C3477-C3487.
32. Ross, K.A.M., P.; Montoya, T.J.; Karasz, E.; Schaller, R.F., *In Preparation: Cold Spray for Mitigation and Repair of Spent Nuclear Fuel Dry Storage Canisters* U.S.D.o. Energy, Editor. 2021.
33. Turner, M.G.-M., E. . *Modeling Galvanic Corrosion*. in *COMSOL Conference*. 2013.

Appendix A

Karasz, E., Montoya, T.D., Taylor, J.M., Ross, K.A., & Schaller, R. F. (2022). Accelerated Corrosion Testing of Cold Spray Coatings on 304L in Chloride Environments. *IHLRWM Conference Proceedings, Fall 2022*.

Accelerated Corrosion Testing of Cold Spray Coatings on 304L in Chloride Environments

Erin Karasz[*,†], Timothy D. Montoya[†], Jason M. Taylor[†], Kenneth A. Ross[‡], and Rebecca F. Schaller[†]

[†]*Sandia National Laboratories, 1515 Eubank Blvd SE, Albuquerque, NM, 87123*
[‡]*Pacific Northwest National Laboratory, 902 Battelle Blvd, WA, 99354*
**corresponding author: ekarasz@sandia.gov*

[leave space for DOI, which will be inserted by ANS]

INTRODUCTION

Since its debut in the 1980's, metal additive manufacturing continues to be an expanding area of research. Many techniques have been, and continue to be, developed. One such technique is cold spray. Cold spray is a technique whereby metal particles are accelerated into a substrate material, propelled by a stream of inert gas at temperatures below the melting temperature of the particles. The inert gas is heated, despite the name of the technique, in order to achieve higher particle velocities. These temperatures are usually under 1100 °C[1]. The metal particles adhere to the substrate through a kinetic deformation process, distinguishing it from other thermal spray and additive manufacturing techniques which rely on melting or sintering. Cold spray also induces compressive residual stresses[2] which are often considered beneficial for preventing stress corrosion cracking[3].

The implementation of materials developed through these techniques has rapidly garnered interest. It has seen application in the medical space for biocompatible implant coatings[4], in the military field for vehicle and aircraft repair[5], and as a corrosion protection and wear resistance coating in nuclear energy[6]. Spent nuclear fuel (SNF) canisters are a promising application space for cold spray.

For dry storage purposes, SNF is placed in stainless steel canisters made of 304 or 316 stainless steel. The canisters are placed in concrete overpacks and passively cooled as ambient air passes through vents in the overpack. These are stored at independent spent fuel storage installations (ISFSI) which are often co-located with the nuclear reactors, many of which are in near-marine environments. As a result, chlorides are deposited from the atmosphere onto the canister surface. As the SNF degrades, the canisters cool and can eventually reach temperatures where the relative humidity (RH) at the canister surface is high enough to deliquesce the deposited chlorides. These chloride-rich brines can induce corrosion on the surface of the canister and subsequently leads to the potential for chloride-induced stress corrosion cracking (CISCC). There are presently over 3,000 canisters containing over 86,000 metric tons of SNF distributed across 77 ISFSIs[7]. At this point in time, there is no permanent geological repository for the SNF. Therefore, research and development of corrosion mitigation and repair solutions for the dry storage canisters are of significant interest. One of the considerations for addressing in-service canisters is the possibility that coating the entire canister surface may not be feasible. As a result, a patch-type application needs to be considered.

In a patch-type application, an exposed junction between the substrate and cold sprayed material exists. This elevates the potential for galvanic corrosion and introduces a region of potentially high corrosion susceptibility at the patch edge. The following work focuses on this region. A full-immersion ASTM G48 Method A ferric chloride pitting test was used to examine accelerated corrosion behavior at the patch edge for nickel and nickel-based alloys cold sprayed onto 304 stainless steel. Nickel-based alloys, like Inconel, are considered to have good corrosion resistance and have historically been considered a low galvanic corrosion risk when paired with 304 stainless steel, making it a promising material for application on SNF canisters.

METHODS AND MATERIALS

A substrate material of wrought 304L was used and cold spray layer of either Inconel 625-2, Super C, or commercially pure Nickel were deposited; compositions are given in Table I. For most of the samples, Nitrogen was used as the accelerating gas, for one sample Helium was used. Two interface types were explored in this work, blended and masked. In the blended case the cold spray layer tapers down to the substrate and in the masked case the drop off to the substrate is abrupt. Samples of each interface, blended and masked, were tested for Inconel-Nitrogen and Nickel-Nitrogen. Super C-Nitrogen and Inconel-Helium are presented only in the blended interface.

Experiments were performed in accordance with ASTM G48 method A, ferric chloride pitting test. The cold spray samples were coated in epoxy on the sides and bottom, as seen in Figure 1, to mimic the surfaces that would be exposed in an actual patch application type scenario. The samples were imaged pre-exposure with a Keyence VHX-7000 digital microscope. Samples were immersed for 72 hours at 22 °C in 6% by mass ferric chloride solution. Post-testing, samples were rinsed with DI water and dried with nitrogen gas. They were imaged post-exposure on a Keyence VHX-7000 before being cross-sectioned, polished to a 1200 grit finish, and re-imaged with the same digital microscope.

Appendix B

Pre-exposure optical images of samples received and characterized but not fully examined for corrosion behavior in FY22 are shown in Figure 27. Table 8 lists all corresponding parameters and cold spray materials.

a) 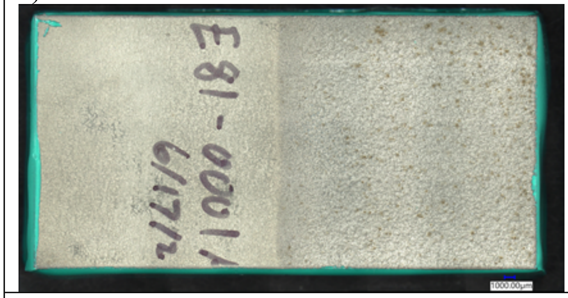 	b) 
c)  	d) 
e) 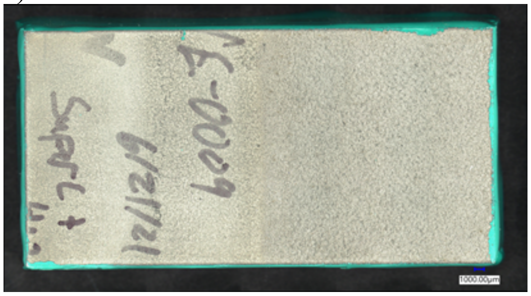 	f) 
g)  	h) 
i)	j)

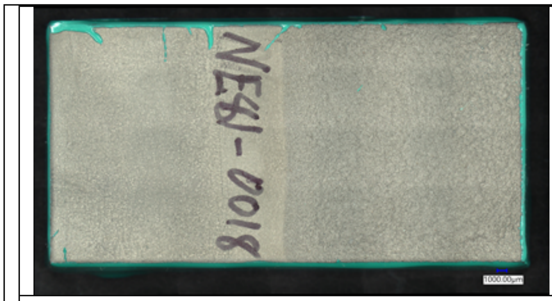NE81-0018 1000.00µm	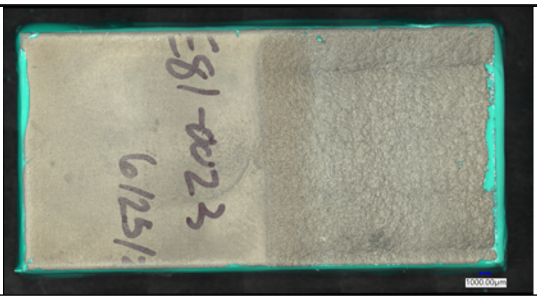E81-0023 6/25/ 1000.00µm
k)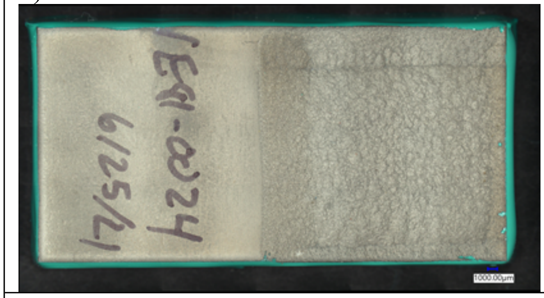NE81-0024 6/25/21 1000.00µm	l)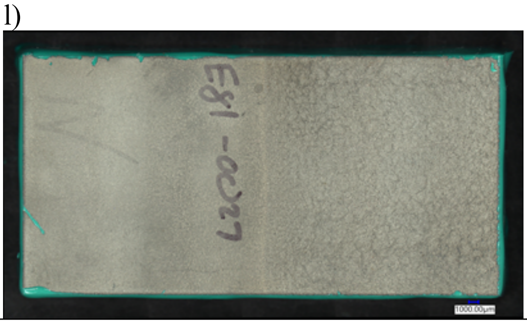E81-0027 1000.00µm
m)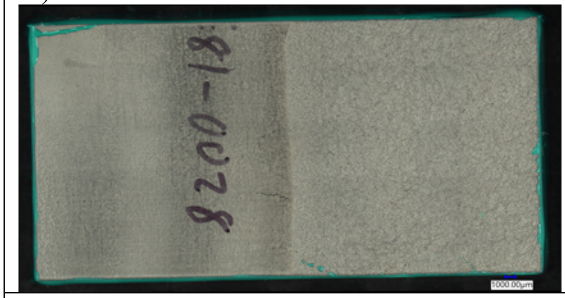81-0028 1000.00µm	n)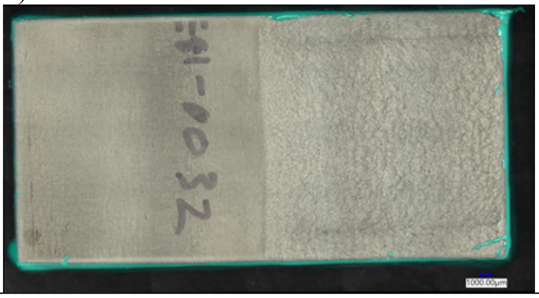E81-0032 1000.00µm
o)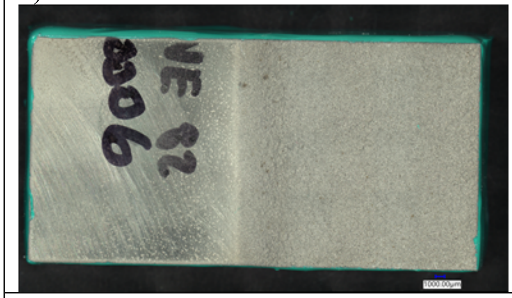NE 82 0006 1000.00µm	p)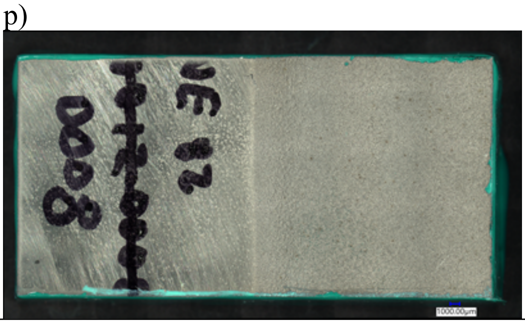NE 82 0008 1000.00µm
q)NE 82 0010 1000.00µm	r)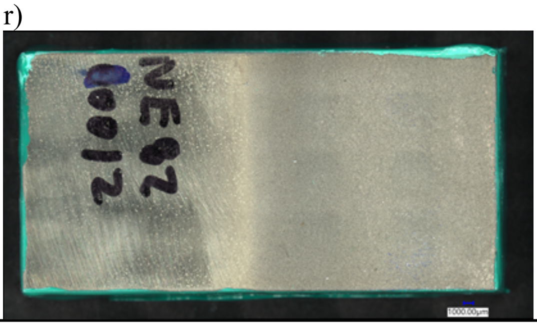NE82 0012 1000.00µm

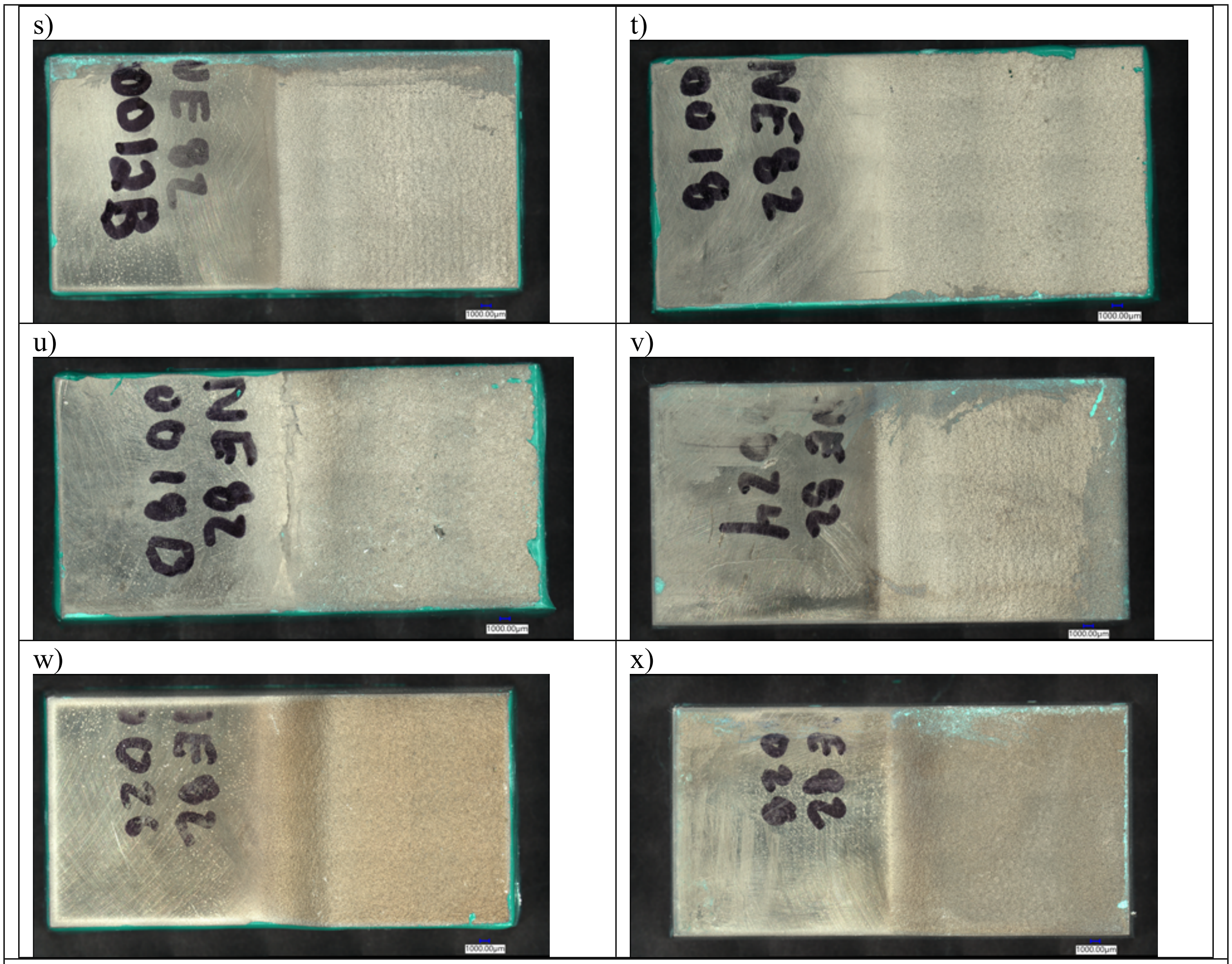

Figure 27. Pre-exposure figures of cold spray samples sent to SNL in FY22. Letters correspond to samples provided in Table 8.

Table 8. FY22 Sample list with spray parameters.

PNNL Sample No.	Figure 27 Letter	Powder	Carrier Gas Pressure (psi)	Carrier Gas Temp (C)	Carrier Gas	Carrier Gas Flow Rate (SLM)/feeder	Deposit thickness (mm)	Deposit thickness per pass (mm)
NE81-0001A	A	75% Super C; 25% CrC 300	900	650	Nitrogen	1127/125	0.3	0.027
NE81-0001B	B	75% SuperC; 25% CrC 300	900	650	Nitrogen	1260/134	0.4	0.036
NE81-0005	C	75% SuperC; 25% CrC 300	400	550	Helium	1223/122	0.7	0.064
NE81-0006	D	75% SuperC; 25% CrC 300	400	650	Helium	1168/122	0.7	0.054
NE81-0009	E	75% SuperC; 25% CrC 410	900	650	Nitrogen	1105/125	0.3	0.027
NE81-0014	F	75% SuperC; 25% CrC 410	400	550	Helium	1269/119	0.8	0.072
NE81-0015	G	75% SuperC; 25% CrC 410	400	650	Helium	1189/133	0.8	0.072
NE81-0017	H	75% SuperC; 25% CrC 410	400	550	Helium	1249/119	1.3	0.062
NE81-0018	I	75% SuperC; 25% CrC 300	900	650	Nitrogen	1069/123	1.1	0.1
NE81-0023	J	75% SuperC; 25% CrC 300	400	550	Helium	1260/122	1.6	0.145
NE81-0024	K	75% SuperC; 25% CrC 300	400	650	Helium	1188/119	1.3	0.118
NE81-0027	L	75% SuperC; 25% CrC 410	900	650	Nitrogen	1082/119	0.8	0.073
NE81-0028	M	75% SuperC; 25% CrC 410	900	650	Nitrogen	1080/117	0.7	0.063
NE81-0032	N	75% SuperC; 25% CrC 410	400	550	Helium	1190/113	1.5	0.136
NE82-0006	O	Duplex SS + 25% CrC 410	400	550	Nitrogen	484	1.82	11.9
NE82-0008	P	Duplex SS + 25% CrC 410	600	650	Nitrogen	689	1.52	28.3
NE82-0010	Q	Duplex SS + 25% CrC 410	400	650	Nitrogen	453	1.41	11
NE82-0012	R	Duplex SS + 25% CrC 410	400	550	Helium	891	0.35	2.5
NE82-0012B	S	Duplex SS + 25% CrC 410	400	550	Helium	887	2.35	15
NE82-0018	T	SS316 + 25% CrC 410	400	550	Nitrogen	487	0.5	2.4
NE82-0018B	U	SS316 + 25% CrC 410	400	550	Nitrogen	496	1.25	6.5
NE82-0018c	Fig 10 A	SS316 + 25% CrC 410	400	530	Nitrogen	515	0.81	4.1
NE82-0020	Fig 10 B	SS316 + 25% CrC 410	600	650	Nitrogen	714	1.02	4.8
lNE82-m0022	Fig 10 C	SS316 + 25% CrC 410	400	650	Nitrogen	468	0.47	2.4
NnE82-00o24	V	SS316 + 25% CrC 410	400	550	Helium	1156	1.46	8.1
NE8p2-0026q	W	SS316	600	650	Helium	1578	4.43	28.4
NE82-r0028	X	SS316	400	650	Helium	1050	1.76	12.7